Cell



# Generation of Functional Human 3D Cortico-Motor Assembloids

## Graphical Abstract

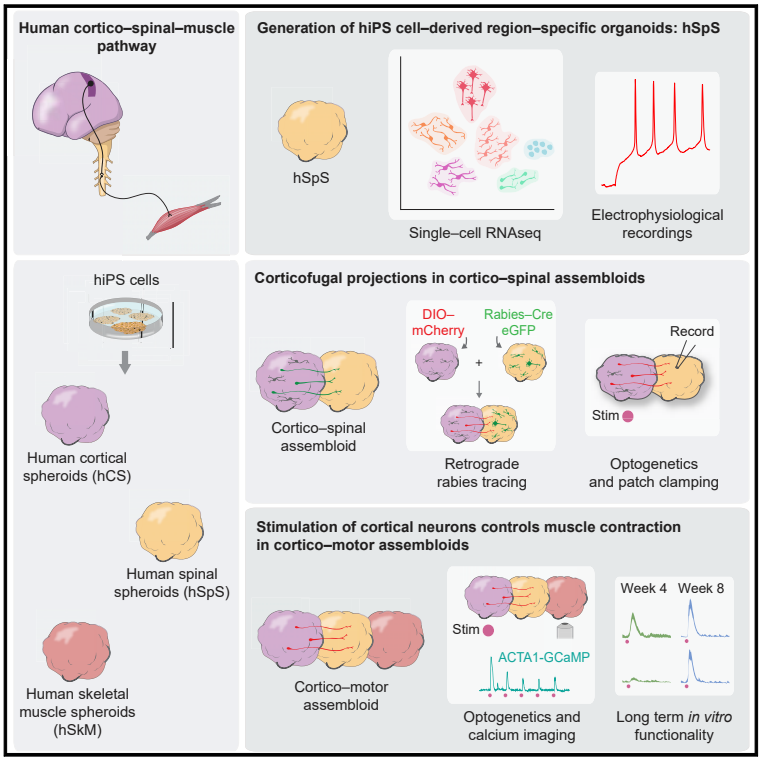


## Highlights

- Generation of hiPS cell-derived 3D spheroids resembling the hindbrain/spinal cord
- Synaptically connected corticofugal projections in fused cortico-spinal assembloids
- Stimulation of cortical neurons controls skeletal muscle in three-part assembloid
- Cellular and functional changes in cortico-motor assembloids maintained long term


## Authors

Jimena Andersen, Omer Revah, Yuki Miura, ..., Hannes Vogel, H. Christina Fan, Sergiu P. Paşca

## Correspondence

spasca@stanford.edu



## In Brief

The assembly of 3D cultures derived from hiPS cells resembling cerebral cortex, hindbrain/spinal cord, and skeletal muscle form neural circuits that can be readily manipulated to model cortical control of muscle contraction *in vitro* long term.


Andersen et al., 2020, Cell *183*, 1–17
December 23, 2020 
https://doi.org/10.1016/j.cell.2020.11.017

CellPress

Please cite this article in press as: Andersen et al., Generation of Functional Human 3D Cortico-Motor Assembloids, Cell (2020), https://doi.org/10.1016/j.cell.2020.11.017

Cell

CellPress

Resource

# Generation of Functional Human 3D Cortico-Motor Assembloids

Jimena Andersen,[1,2] Omer Revah,[1,2] Yuki Miura,[1,2] Nicholas Thom,[1] Neal D. Amin,[1,2] Kevin W. Kelley,[1,2] Mandeep Singh,[1,2] Xiaoyu Chen,[1,2] Mayuri Vijay Thete,[1] Elisabeth M. Walczak,[3] Hannes Vogel,[4] H. Christina Fan,[3] and Sergiu P. Paşca[1,2,5,*]

[1]Department of Psychiatry and Behavioral Sciences, Stanford University, Stanford, CA 94305, USA
[2]Stanford Brain Organogenesis Program, Wu Tsai Neurosciences Institute, Stanford University, Stanford, CA 94305, USA
[3]BD Biosciences, 4040 Campbell Ave Suite 110, Menlo Park, CA 94025, USA
[4]Departments of Pathology and Pediatrics, Stanford University, Stanford, CA 94305, USA
[5]Lead Contact
*Correspondence: spasca@stanford.edu
https://doi.org/10.1016/j.cell.2020.11.017

## SUMMARY

Neurons in the cerebral cortex connect through descending pathways to hindbrain and spinal cord to activate muscle and generate movement. Although components of this pathway have been previously generated and studied *in vitro*, the assembly of this multi-synaptic circuit has not yet been achieved with human cells. Here, we derive organoids resembling the cerebral cortex or the hindbrain/spinal cord and assemble them with human skeletal muscle spheroids to generate 3D cortico-motor assembloids. Using rabies tracing, calcium imaging, and patch-clamp recordings, we show that corticofugal neurons project and connect with spinal spheroids, while spinal-derived motor neurons connect with muscle. Glutamate uncaging or optogenetic stimulation of cortical spheroids triggers robust contraction of 3D muscle, and assembloids are morphologically and functionally intact for up to 10 weeks post-fusion. Together, this system highlights the remarkable self-assembly capacity of 3D cultures to form functional circuits that could be used to understand development and disease.

## INTRODUCTION

The main function of the cortico-motor pathway is the regulation of neural activity in the hindbrain and spinal cord to generate coordinated movement (Lemon, 2008). Corticofugal glutamatergic neurons in the cerebral cortex send long-range axons to modulate networks in the hindbrain and spinal cord to ultimately induce muscle contraction (Kiehn, 2016; Lodato and Arlotta, 2015; Shim et al., 2012; ten Donkelaar et al., 2004) (Figure 1A). Damage or degeneration of the cortico-motor circuit following traumatic injury, amyotrophic lateral sclerosis, or autoimmune disorders result in severe motor dysfunction (Blesch and Tuszynski, 2009). Recent evidence points at primate-specific reorganization and connectivity of the cortico-spinal pathway, including the presence of direct monosynaptic cortico-spinal connections, which may be related to corticalization of motor control and the evolution of dexterity (Gu et al., 2017; Lemon, 2008; Sousa et al., 2017). These species-specific differences are further highlighted by challenges in translating findings from animal models (Kaiser and Feng, 2015; Philips and Rothstein, 2015; van der Worp et al., 2010). Therefore, direct access to human cortico-spinal-muscle circuits has the potential to accelerate our understanding of motor disorders.

Induced pluripotent stem cells hold promise in building personalized disease models. Although components of the cortico-spinal-motor pathway have been generated or studied in isolation (Ogura et al., 2018; Sances et al., 2016; Shi et al., 2018; Steinbeck et al., 2016), the *in vitro* derivation and assembly of this three-part system have not yet been achieved with human cells. We have previously developed an approach to model complex cellular interactions during human brain development by specifying region-specific spheroids or organoids and then fusing them *in vitro* to generate three-dimensional (3D) assembloids (Birey et al., 2017; Paşca, 2019; Sloan et al., 2018). Long-range neural projections have been observed in a cortico-thalamic assembloid (Xiang et al., 2019), in organotypic mouse co-cultures (Takuma et al., 2002) and in a preparation that used sliced cortical organoids and rodent spinal cord explants (Giandomenico et al., 2019). However, *in vitro* derivation and assembly of a functional multi-synaptic circuit from human cells have not been achieved.

Here, we leverage a modular assembloid approach to separately generate and then functionally integrate the components of a cortico-motor circuit. More specifically, we find that human-induced pluripotent stem (hiPS) cell-derived region-specific spheroids form physiologically relevant connections when assembled together. Spheroids resembling the cerebral cortex form long-range functional connections with spheroids resembling the hindbrain/cervical spinal cord, and these in turn project

Please cite this article in press as: Andersen et al., Generation of Functional Human 3D Cortico-Motor Assembloids, Cell (2020), https://doi.org/10.1016/j.cell.2020.11.017



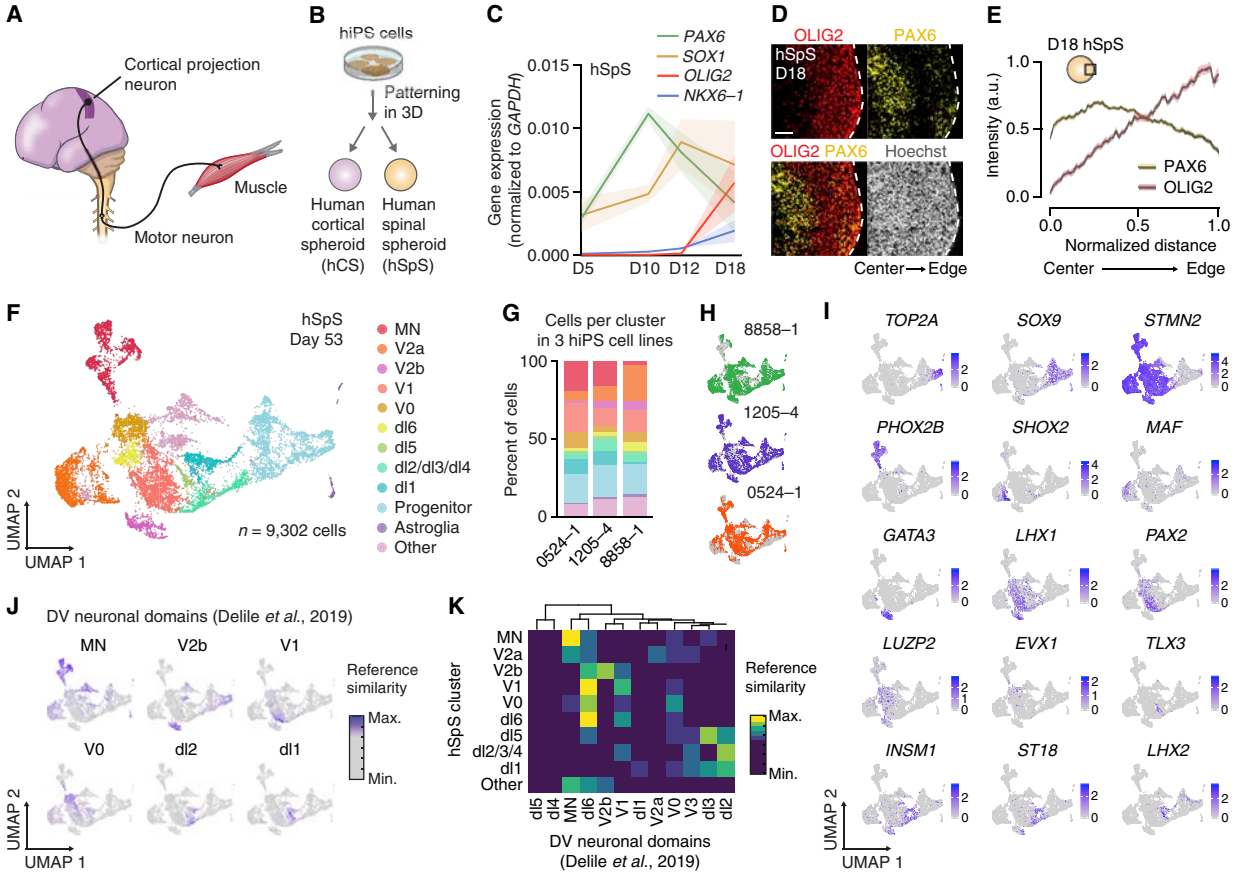


**Figure 1. Generation of hSpS from hiPS Cells**

(A) Schematic illustrating the main cellular components of the cortico-motor system.

(B) Schematic illustrating the generation of human cortical spheroids (hCS) and human spinal spheroids (hSpS) from hiPS cells.

(C) Gene expression (RT-qPCR) of spinal cord-related gene markers at 5, 10, 12, and 18 days in hSpS. Data represent mean ± SEM (n = 3 hiPS cell lines from 1 differentiation; two-way ANOVA, interaction $F[9,32] = 3.29$, $p = 0.005$).

(D) Representative immunocytochemistry images of OLIG2 and PAX6 in hSpS at day 18. Scale bar, 50 μm.

(E) Fluorescence intensity analysis showing expression of OLIG2 and PAX6 plotted versus the distance from the center (left) to the edge (right) of hSpS at day 18. Black traces represent the mean and shaded bars represent the SEM (n = 20 hSpS derived from 3 hiPS cell lines from 2 separate differentiations, with 2–4 cryosections quantified per hSpS).

(F) UMAP visualization of single cell gene expression of hSpS at day 53 (n = 9,302 cells from 3 hiPS cell lines).

(G) Graph showing the percentage of cells in each of the three hiPS cell lines used for this experiment belonging to each cluster in hSpS.

(H) UMAP plot showing cells separately colored by the hiPS cell line they were derived from.

(I) UMAP plots showing gene expression of selected hSpS cluster-specific markers. Colored scale shows normalized gene expression data, log (counts per 10,000).

(J) hSpS UMAP plots colored by reference similarity spectrum (RSS) to selected single-cell RNA sequencing (RNA-seq) clusters from mouse spinal cord from Delile et al. (2019).

(K) Hierarchical clustering showing RSS analysis of hSpS clusters to single-cell RNA-seq clusters from mouse developing spinal cord neuronal clusters from Delile et al. (2019).

*(legend continued on next page)*

Please cite this article in press as: Andersen et al., Generation of Functional Human 3D Cortico-Motor Assembloids, Cell (2020), https://doi.org/10.1016/j.cell.2020.11.017



and connect with human skeletal muscle. Importantly, these cortico-motor assembloids can be used to trace anatomical and functional connectivity, can be maintained long term *in vitro* to capture cellular and functional changes, and can be manipulated optogenetically or pharmacologically at multiple levels to control human muscle contraction.

## RESULTS

### Generation of Hindbrain/Cervical Spinal Cord Spheroids from Pluripotent Stem Cells

We first generated spheroids resembling the human hindbrain/cervical spinal cord (hSpS) starting from hiPS cells (Figure 1B; Table S1 summarizes the color-coded use of n = 9 hiPS cell lines in various experiments). Specification of the progenitor domains in the hindbrain and spinal cord relies on signaling molecules like WNT and retinoic acid (RA) secreted along the rostro-caudal axis, and sonic hedgehog (SHH) along the dorso-ventral axis (Alaynick et al., 2011; Goulding, 2009; Jessell, 2000; Kiehn, 2006) (Figures S1A and S1B). A number of groups have developed protocols to generate spinal motor neurons by modulating these pathways *in vitro* (Amoroso et al., 2013; Butts et al., 2019; Gouti et al., 2014; Wichterle et al., 2002). To establish hSpS, we designed a combinatorial approach (12 conditions) to test FGF-2, RA, WNT, and SHH modulators at varying concentrations following neural ectoderm specification (Figure S1C). Briefly, hiPS cell colonies were lifted using the enzyme dispase, moved to ultra-low attachment plates to form spheroids, and exposed to dual SMAD inhibition (Paşca et al., 2015; Sloan et al., 2018). Starting on day 4, spheroids were exposed to the WNT activator CHIR-99021 (3 μM) and to 20 ng/mL epidermal growth factor (EGF) from day 6 onward. Spheroids also received a combination of RA (0.01 or 0.1 μM) and FGF-2 (0, 10, or 20 ng/mL) from day 6, and the SHH activator smoothened agonist (SAG; 0, 0.01, 0.1 or 1 μM) from day 11. To determine the fate of the resulting spheroids in each condition, we assessed gene expression at day 20 (Figures S1D–S1F; primers listed in Table S1). Exposure to high levels of RA and low levels of FGF-2 results in more rostral fates (Figure S1D; *HOXA2*, p = 0.002), whereas exposure to low levels of RA and high levels of FGF-2 yields more caudal fates (Figure S1D; *HOXC9*, p = 0.002). Moreover, high SAG exposure is associated with higher expression of ventral marker genes (Figures S1E and S1F; *OLIG2*, p = 0.001; *NKX6-1*, p = 0.002; *CHX10*, p = 0.007; and *ISL1*, p = 0.01). Ventral and dorsal identities were also confirmed by immunocytochemistry in hSpS cryo-sections (Figure S1G; antibodies listed in Table S1). Based on the overall diversity of domain-specific markers expressed, we chose to pursue condition 8 for further experiments (0.1 μM RA, 0.1 μM SAG, and 10 ng/mL FGF-2) (Figure S1H). Other conditions, such as condition 12, showed higher expression of motor neuron markers, but had lower expression of interneuron markers, which are essential for hindbrain/spinal cord circuitry. In condition 8 (hSpS), the neuroectodermal markers *SOX1* and *PAX6* peaked at day 10, followed by an increase in the expression of *OLIG2* and *NKX6-1* from day 12 (Figure 1C; interaction p = 0.005, gene p < 0.0001, time p = 0.01).

*In vivo*, hindbrain/spinal cord progenitors are organized in a stereotypical pattern (Dasen and Jessell, 2009). To explore organization in day 18 hSpS, we used immunohistochemistry for the ventral marker OLIG2 and the medial marker PAX6. We found that OLIG2 was more highly expressed toward the edge of the hSpS, whereas PAX6 showed the opposite pattern, with higher expression toward the center (Figures 1D and 1E). We next further characterized OLIG2$^+$ progenitors, which give rise to motor neurons (Figures S1I–S1L), and found that ~40% of OLIG2$^+$ cells co-expressed the marker NKX2.2 and ~15% co-expressed NKX6.1 (Figure S1L). This pattern of expression suggests the presence of hindbrain and spinal cord motor neuron progenitor populations in hSpS (Guthrie, 2007).

Next, we tested whether the presence of the Notch pathway modulator DAPT (Borghese et al., 2010) changed the proportions of cell types present in hSpS (Figures S2A and S2B). For this, we performed single-cell transcriptional profiling (Fan et al., 2015) in day 45 hSpS that were differentiated in the presence or absence of DAPT from day 19 to day 24 (Figure S2C) (n = 7,888 cells; BD Rhapsody). Analysis of cells using the t-distributed stochastic neighbor embedding (*t*-SNE) approach (van der Maaten and Hinton, 2008) identified several domains, including groups of GABAergic, glycinergic and glutamatergic interneurons (4, 5, 7, 8, and 9), as well as a mixed neuronal cluster (6), and a motor neuron cluster (10) (Figures S2C and S2D; Table S1). When differentiated in the presence of DAPT, although overall similar to the unexposed condition (hSpS$^{(-)DAPT}$; $R^2$ = 0.85, p < 0.0001), hSpS contained a ~3-fold increase in the proportion of motor neurons as well as a 4-fold decrease in the proportion of an undefined mixed neuronal population (Figures S2E and S2F). We further validated the presence of these neuronal and glial populations by performing real-time qPCR for a set of domain-specific markers in day 30 hSpS and hSpS$^{-DAPT}$ derived from 5 hiPS cell lines in 4 separate differentiation experiments (Figures S2G–S2I), and confirmed expression of some of these genes by immunocytochemistry in cryo-sections (Figures S2J and S2K). Based on these data, we chose to use the hSpS condition that included DAPT exposure.

One of the challenges of using organoids for studying development and disease is the reproducibility of differentiation between hiPS cell lines. We have previously demonstrated high reliability in the generation of organoids resembling the dorsal forebrain (Yoon et al., 2019), and to investigate this aspect in hSpS, we performed droplet-based single-cell transcriptomics at day 53 (10x Genomics Chromium) in three different hiPS cell lines that were differentiated in parallel (n = 9,302 cells). We first used the uniform manifold approximation and projection (UMAP) dimensionality reduction technique to visualize cells and determine their identity (Figure 1F; Figure S3A shows *t*-SNE reduction; Table S1 shows the top 50 differentially expressed genes per cluster). We found that cells grouped into 12 main clusters, and when we compared the proportions of cells in each cluster

(L and M) Dot plots showing the expression of selected domain-specific and neurotransmitter identity-related genes (L), and expression of *HOX* genes (M) in each of the neuronal clusters in hSpS. The size of the circle represents the percent of cells expressing each gene per cluster.
See also Figures S1, S2, and S3 and Table S1.

Please cite this article in press as: Andersen et al., Generation of Functional Human 3D Cortico-Motor Assembloids, Cell (2020), https://doi.org/10.1016/j.cell.2020.11.017



across lines, we found that cell diversity was overall similar (Figures 1G, 1H, and S3B). We also compared expression of all genes across lines and found that they were highly correlated (8858-1 versus 0524-1 $R^2$ = 0.98, 8858-1 versus 1205-4 $R^2$ = 0.99, and 1205-4 versus 0524-1 $R^2$ = 0.98, Figure S3C). Similarly, we found that gene expression in each domain was highly correlated across lines (Figure S3D).

Next, we explored hSpS cell cluster identity and found they included progenitors expressing *SOX9* and *TOP2A*, astroglia, and several neuronal domains including a dorsal group of cells expressing *LHX2*, *INSM1*, *ST18*, and *TLX3* (clusters dI1, dI2/3/4, dI5, and dI6), four ventral clusters that showed expression of *LHX1*, *PAX2*, *EVX1*, *SHOX2* and *GATA3* (V0, V1, V2a, and V2b), and a group of motor neurons expressing *ISL1*, *PRPH*, and *PHOX2B* (MN) (Figures 1I and 1L). We did not find a clear V3 domain with this analysis, and we found no non-ectodermal cells, however, we identified a group of neural cells that we could not define based on known marker genes. One hiPS cell line (8858-1) had a higher proportion of V2a neurons at the expense of motor neurons (Figure 1G). The balance between V2a interneurons and motor neurons is known to be linked (Thaler et al., 1999), and loss of motor neurons in Olig1/2 knockout mice results in a dramatic increase of $Chx10^+$ V2a interneurons (Zhou and Anderson, 2002). Real-time qPCR for *ISL1* and *CHX10* showed that out of 16 samples from 5 lines in 4 differentiations, 2 had higher expression of *CHX10* compared to *ISL1* (Figure S2G). Variation in the state of hiPS cell lines can lead to divergent neuronal biases (Micali et al., 2020), and real-time qPCRs for these two markers at ~day 30 in hSpS could be implemented as a quality control step.

To further validate the cluster assignment, we compared hSpS to annotated neuronal clusters from the developing mouse spinal cord (Delile et al., 2019) using reference similarity spectrum (RSS) analysis (Kanton et al., 2019). We found that, overall, cluster annotation in hSpS matched previously annotated spinal cord clusters (Figures 1J and 1K) (Delile et al., 2019; Rosenberg et al., 2018; Sathyamurthy et al., 2018). Some dorsal clusters appeared to be less correlated compared to ventral clusters, which may be explained by the lack of dorsalizing signals in hSpS. We also looked at neurotransmitter identity in the neuronal clusters and we found that it broadly matched that described in the literature (Delile et al., 2019) and included glutamatergic (*SLC17A6*$^+$), GABAergic (*GAD1*$^+$, *GAD2*$^+$ or *SLC32A1*$^+$), glycinergic (*SLC6A5*$^+$), and cholinergic (*SLC5A7*$^+$ or *SLC18A3*$^+$) cells (Figure 1L). Genes encoding cell adhesion and neuronal guidance molecules, such as *PCDH7*, *NRXN3*, and *ROBO3*, were also expressed in a domain-specific manner (Figure S3E).

To explore rostro-caudal identity of hSpS, we examined the expression of HOX genes in hSpS and found expression of *HOXB4*, *HOXC4*, and *HOXB5*, suggestive of caudal hindbrain/cervical spinal cord identity (Figures 1M and S3F). Moreover, RSS analysis comparing hSpS to different CNS regions in the mouse (Zeisel et al., 2018) showed that hSpS was most closely correlated to hindbrain cell types, further validating the identity of hSpS (Figures S3G and S3H). However, direct comparison to human developing hindbrain/spinal cord in the future could better address these questions.

Next, to further characterize motor neurons in hSpS, we re-clustered the MN cluster from the single cell gene expression analysis. We found that MN subdivided into at least 6 groups (Figures S3I–S3K). Most of these cells expressed the motor neuron marker *PHOX2B*, but did not express the visceral motor neuron marker *TBX20*, suggesting motor neurons in hSpS have a largely somatic identity (Figure S3M). MN cluster 6 was negative for *PHOX2B* and positive for *ISL1/2* and *HB9* (*MNX1*), indicating a limb-innervating lateral motor column-like identity (Figures S3I–S3M).

We also confirmed the presence of cholinergic motor neurons in hSpS by immunocytochemistry for the enzyme that catalyzes the biosynthesis of the neurotransmitter acetylcholine (CHAT), the vesicular acetylcholine transporter VACHT, the neurofilament SMI-32, and the transcription factors HB9, ISL1, and PHOX2B (Figures 2A, 2B, and S4A–S4F), and by electrophysiological recordings using an Hb9::GFP reporter (Figures 2C and 2D). We also observed the presence of ventral neuronal domains in hSpS by immunohistochemistry at day 45 (Figures 2E, 2F, and S4G), as well as the presence of astrocytes and oligodendrocytes at day 75 (Figure 2G). Whereas spinal cord progenitors are organized in a well-defined laminar pattern during development, post-mitotic neurons in the spinal cord do not appear to maintain this organization at later stages (Lai et al., 2016).

## Generation of Cortico-Spinal Assembloids

We previously described the generation of 3D spheroids resembling the cerebral cortex (human cortical spheroids [hCS]) (Birey et al., 2017; Paşca et al., 2015; Sloan et al., 2017, 2018), which contain deep and superficial glutamatergic neurons. We verified expression of cortico-spinal-associated markers in hCS, including *FEZF2*, *BCL11B* (*CTIP2*), and *SOX5*, using single-cell profiling of hCS (Birey et al., 2017) and found a population of cells co-expressing these genes in the glutamatergic neuron cluster but not in a subpallial-derived GABAergic cluster (Figure S5A). Moreover, we confirmed the expression of some these genes by real-time qPCR from day 45 to day 130 (Figure S5C), as well as by immunocytochemistry with antibodies that we validated in slices of human cortical tissue at post-conception week 17 (PCW17) (Figures S5D and S5E). Importantly, we found no expression of cholinergic markers *CHT1* and *VACHT* in hCS (Figure S5B).

To generate cortico-spinal assembloids, we fused hSpS with an hCS that had been infected with an AAV-hSYN1::eYFP reporter (Figure 3A). Live imaging at 5 days after fusion (daf) showed processes derived from cells in the hCS extending into hSpS (Figure 3B; Video S1). At 30 daf, immunocytochemistry for YFP showed extensive hCS-derived projections in hSpS (Figure 3C). Quantification of the $eYFP^+$-covered area in hSpS in intact hCS-hSpS assembloids showed a progressive increase of eYFP over time (5 daf versus 10 daf $p = 0.009$; 5 daf versus 20 daf $p < 0.0001$; Figures 3D, S5F, and S5G for examples of hCS-hSpS assembloids at 20 daf), and this was not observed to the same extent in hCS-hCS assembloids (5 daf versus 10 daf $p > 0.9$; 5 daf versus 20 daf $p = 0.06$; Figures 3E, S5H, and S5I). Immunohistochemistry in hCS-hSpS assembloids at 28 daf showed that hCS-derived eYFP processes often project toward $ISL1^+$ cell clusters (Figure 3F). We also generated hSpS using a fluorescently labeled CAG::EGFP hiPS cell line to examine reciprocal hSpS interactions with hCS and found that hSpS cells sometimes projected into hCS but seldom migrated (Figure S5J).

Please cite this article in press as: Andersen et al., Generation of Functional Human 3D Cortico-Motor Assembloids, Cell (2020), https://doi.org/10.1016/j.cell.2020.11.017



CellPress

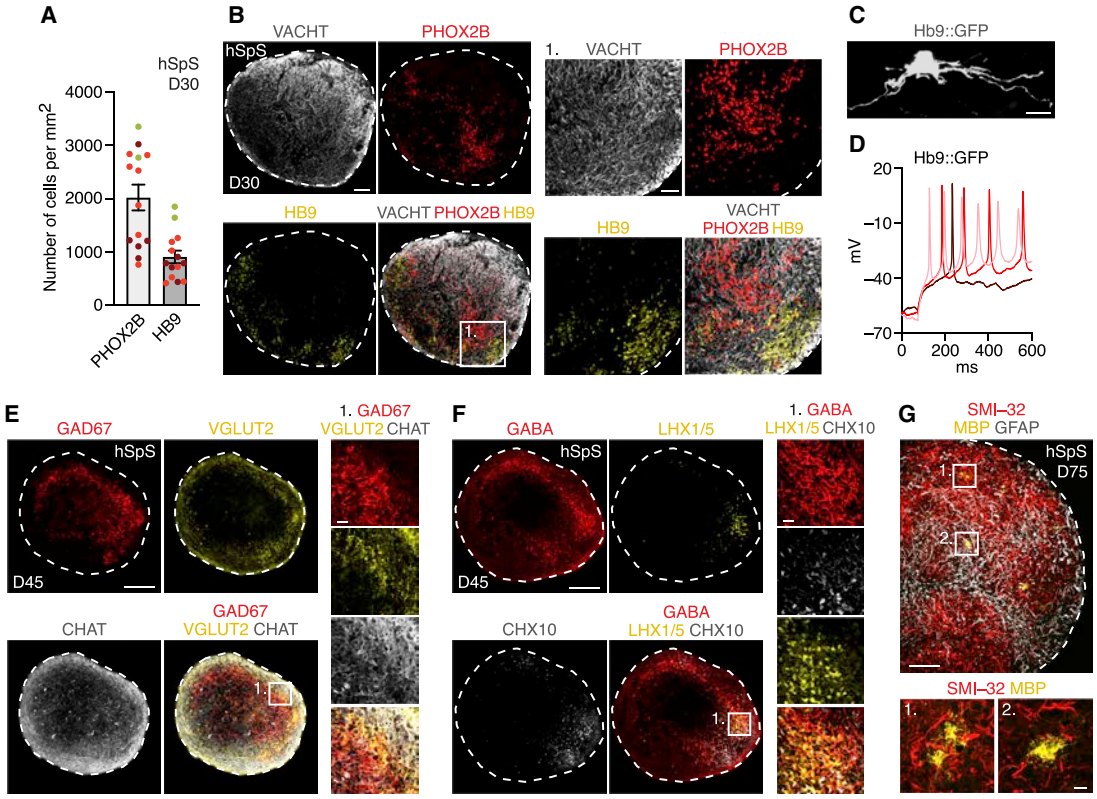


**Figure 2. Characterization of hSpS**

(A) Quantification of the total number of cells expressing PHOX2B or HB9 per area ($mm^2$) in 16 μm hSpS cryosections at day 30. Data represent mean ± SEM (n = 14 hSpS derived from 3 hiPS cell lines from 1–2 differentiations, with 2–4 cryosections quantified per hSpS).

(B) Representative immunohistochemistry images of day 30 hSpS.

(C) Immunocytochemistry showing a lenti-Hb9::$GFP^+$ neuron in an hSpS cryosection.

(D) Whole-cell current-clamp recording from an Hb9::GFP cell showing action potential generation in response to depolarizing current injections.

(E and F) Representative immunohistochemistry images of neuronal domains with diverse neurotransmitter identities on day 45 hSpS.

(G) Immunocytochemistry in day 75 hSpS showing expression of the astrocyte marker GFAP and the oligodendrocyte marker MBP.

Scale bars, 10 μm (C), inset in (G), 20 μm (insets in E and F), 50 μm (inset in B), 100 μm (B and G), and 200 μm (E and F).

See also Figure S4 and Table S1.

Similarly, we did not observe hSpS-derived Hb9 cells migrating into hCS in hCS-hSpS assembloids where hSpS had been infected with Hb9::mCherry (Figure S5K).

## Viral Tracing, Optogenetics, and Calcium Imaging in Cortico-Spinal Assembloids

To characterize the specificity of hCS-derived projections, we used a retrograde rabies tracing approach (Figure 3G). We separately infected hSpS with a ΔG-rabies virus carrying Cre-eGFP and with an AAV carrying the rabies glycoprotein (G) required for *trans*-synaptic spread (Coulon et al., 1983; Etessami et al., 2000), and hCS with an AAV encoding mCherry under a double-floxed inverse orf (DIO-mCherry). After 6–7 days of infection, day ~80 hCS and days ~40–50 hSpS were assembled and expression of GFP and mCherry was examined at 31 daf. We predicted infected neurons in hSpS would express GFP from the rabies-Cre virus, and hCS neurons would co-express GFP and mCherry following rabies-Cre retrograde transport and recombination. We observed extensive expression of GFP in hSpS and cells co-expressing GFP and mCherry in hCS (Figures 3H and S5L). We found that ~95% of the $GFP^+$/$mCherry^+$ cells in hCS co-expressed the neuronal marker MAP2 and fewer than 4% expressed the glial lineage marker GFAP (Figures 3I, 3J, S5M, and S5N). Corticofugal projection neurons, which include cortico-spinal projecting cells, express CTIP2 and are mainly located in deep layers of the cerebral cortex, whereas neurons located in superficial layers express BRN2 and project to the contra-lateral cortex (Greig et al., 2013). To verify the projection identity of $GFP^+$/$mCherry^+$ cells, we quantified the proportion of cells that co-expressed either CTIP2 or BRN2. We found that almost 60% of all $GFP^+$/$mCherry^+$ cells co-expressed the corticofugal marker CTIP2, and only ~12% co-expressed BRN2 (Figures 3K–3M and S5O), although the relative proportions of these cell types were not different in hCS at this *in vitro* stage (Figure 3N).

We next used optogenetics and calcium imaging to probe whether hCS-derived projections formed functional connections. We used AAV viruses to separately deliver, before

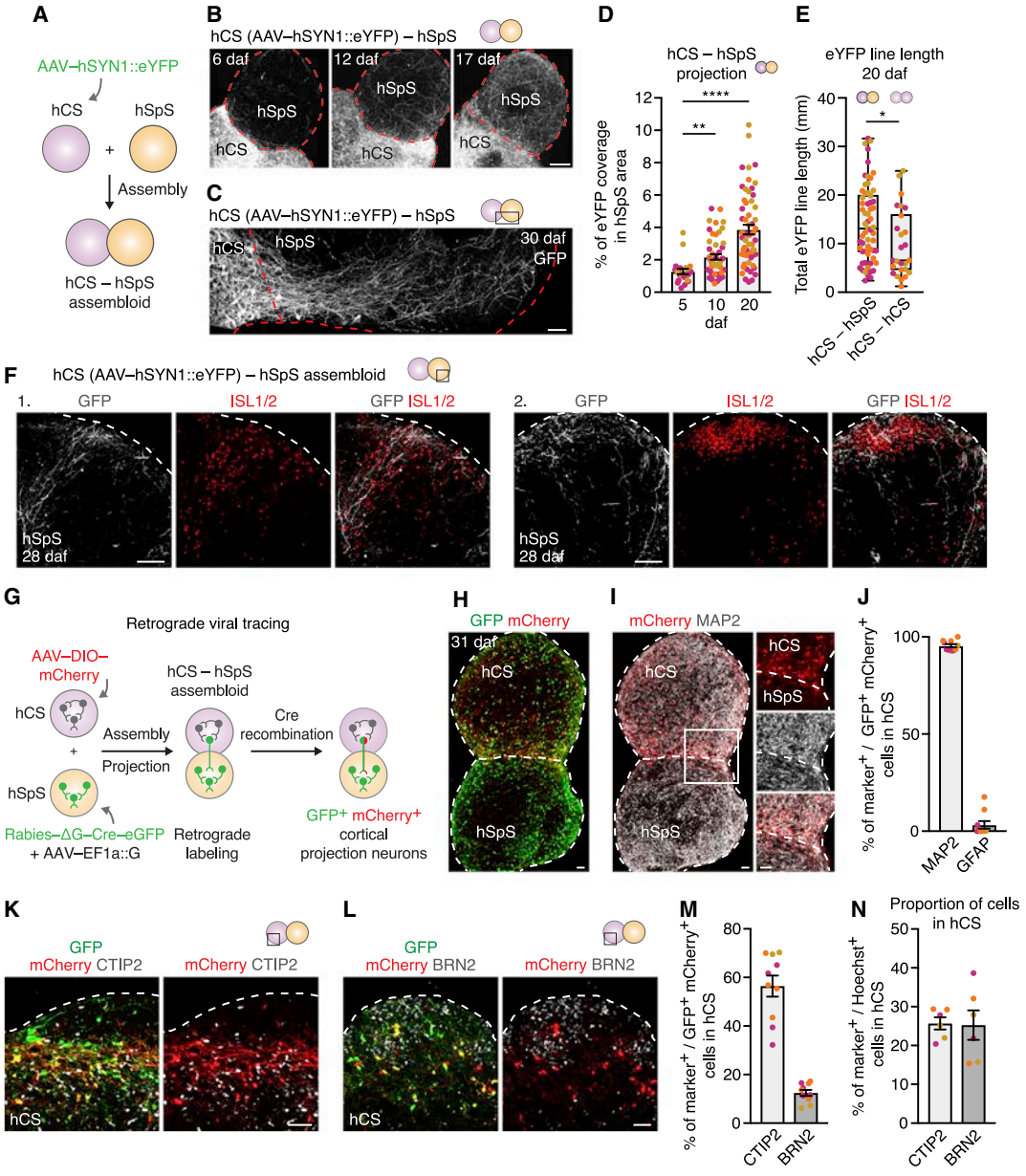


**Figure 3. Generation of hCS-hSpS Assembloids and Characterization of Cortico-Spinal Projections**

(A) Schematic illustrating the fusion of hCS and hSpS to form hCS-hSpS assembloids.

(B) Representative images of intact hCS-hSpS assembloid showing hCS-derived hSYN1::eYFP projections 6, 12, and 17 days after fusion (daf). See Video S1 for live imaging of AAV-hSYN1::eYFP projection at 5 daf.

(C) Immunocytochemistry of hCS-hSpS assembloid 30 days after fusion (daf).

(D) Quantification of hCS-derived eYFP coverage in hSpS area at 5, 10, and 20 daf in hCS-hSpS assembloids (n = assembloids from 3 hiPS cell lines from 3 separate differentiations, Kruskal-Wallis test $p < 0.0001$ with Dunn's multiple test comparison: $^{**}p = 0.009$ for 10 daf versus 5 daf, $^{****}p < 0.0001$ for 20 daf versus 5 daf).

(E) Quantification of total eYFP line length on the projection side of hCS-hSpS or hCS-hCS assembloids at 20 daf (n = 3 hiPS cell lines from 1–2 differentiations; Mann-Whitney test: $^{*}p = 0.01$). Boxplot shows median and 75$^{th}$ and 25th$^{th}$ percentiles, and whiskers show minimum (min.) and maximum (max.) values.

(F) Immunohistochemistry images in hCS-hSpS assembloids at 28 daf showing eYFP projections overlapping with ISL1$^{+}$ cell clusters.

(G) Schematic detailing retrograde viral tracing experiment in hCS-hSpS assembloids.

(H) Immunocytochemistry of hCS-hSpS assembloid at 31 daf showing co-expression of GFP and mCherry on the hCS side.

(I) Immunocytochemistry of hCS-hSpS assembloid at 31 daf showing expression of mCherry and MAP2.

(J) Quantification of the percentage (%) of GFP$^{+}$ and mCherry$^{+}$ cells on the hCS side that co-express MAP2 or GFAP (n = 10 assembloids from 3 hiPS cell lines from 1–2 separate differentiations, with 2–3 cryosections quantified per assembloid).

*(legend continued on next page)*

Please cite this article in press as: Andersen et al., Generation of Functional Human 3D Cortico-Motor Assembloids, Cell (2020), https://doi.org/10.1016/j.cell.2020.11.017





assembly, the light-sensitive opsin Chrimson (Chrim, AAV-hSYN1-ChrimsonR-tdT) (Klapoetke et al., 2014) into hCS and the genetically encoded calcium indicator GCaMP7s (AAV-hSYN1-jGCaMP7s) into hSpS (Figures 4A and 4B). We then imaged calcium transients (10 Hz) at 29–46 daf, while delivering short (100 ms) pulses of red light (625 nm) onto hCS using a fiber optic. We found that neurons in hSpS in 4 out of 10 assembloids responded with calcium spikes that followed the stimulus after ~200 ms (Figures 4C and 4D). To confirm the relationship between stimulation and calcium responses, we compared the stimulus-triggered change in amplitude (ΔF/F) to random time-locked ΔF/F in the same cell. We found that the median amplitude of the response was ~5 times higher for real stimulation compared to randomly selected time points (n = 16 cells, p = 0.0005); Figure 4E). These responses were blocked by application of the ionotropic glutamate receptor blockers NBQX (20 μM) and APV (50 μM) (Figures 4D and 4F), indicating glutamatergic transmission from hCS to hSpS.

To verify that cortical neurons in hCS are synaptically connected to motor neurons in hSpS, we performed voltage clamp recordings in slices of hCS-hSpS assembloids. We infected hCS with AAV1-Syn1::Chrimson-mCherry and used the Hb9::GFP reporter in hSpS to visually identify motor neurons (Figures 4G and 4H). We found that consecutive light stimulation to the area surrounding $Hb9^+$ cells could result in reliable post-synaptic currents (Figure 4I; 2 out of 30 recorded cells in 4 assembloids). These responses could be blocked by application of TTX, indicating that they have been triggered by action potentials in axons of hCS neurons by mono- or di-synaptic connections. Together, these assays indicate that corticofugal neurons in hCS synaptically connect with neurons in hSpS.

## Functional Assembly of Spinal Spheroids with Muscle

The functional output of the cortico-motor circuit is muscle contraction through motor neuron activity. To probe the ability of hSpS to mediate muscle contraction, we dissected mouse limb buds at embryonic day 11.5 (E11.5) before spinal cord axonal innervation and directly assembled them with hSpS derived from a TUBA1B-mEGFP hiPS cell line. We observed extensive projections from the hSpS into the limb bud upon assembly (Figure 5A). Moreover, limb buds displayed spontaneous contractions when assembled with hSpS, but not when kept in isolation or when assembled with hCS ($\chi^2$ test, p = 0.02; Figure 5B). Activity in hSpS-limb assembloids persisted for at least 2 weeks *in vitro* and was completely blocked by addition of the acetylcholine receptor antagonist curare (100 μM; $\chi^2$ test, p = 0.02, Figure 5B; Video S2, sequence 1).

Next, we probed the ability of hSpS to modulate the activity of human muscle cells. To achieve this, we used human skeletal myoblasts (hSkM) (Figure S6A) derived from adult muscle biopsies. Differentiated myotubes expressed markers of mature skeletal muscle, such as desmin (DES), titin (TTN), and the heavy chain myosin (MyHC), and became multinucleated (Figures S6B and S6C). We placed hSpS on top of hSkM grown in 2D adherent cultures (Figure 5C), and within a week, hSpS projected out to cover muscle cells (Figure 5D). Using live imaging with the calcium indicator Cal-590, we found that the proportion of active hSkM doubled in hSpS-hSkM in comparison to hSkM in isolation or co-cultured with hCS (hSpS-hSkM versus hSkM p = 0.01; Figures 5E and S6D; Video S2, sequence 2). This effect was observed mainly in hSkM within 1 mm of hSpS (hSkM versus hSpS-hSkM <1 mm, p < 0.0001; Figures S6E and S6F) and was blocked by curare (Figure 5E). Immunocytochemistry of hSkM after co-culture with hSpS revealed binding of bungarotoxin (BTX) (Figure S6G), a peptide that binds with high affinity to nicotinic acetylcholine receptors at neuromuscular junctions (NMJs).

We then generated 3D hSkM by combining dissociated proliferative hSkM in an extracellular matrix within a silicone well (Figure 5F; see STAR Methods for details). We placed an hSpS and a 3D hSkM in close proximity on top of a 6-well transwell insert to generate hSpS-hSkM assembloids (Figures 5G, 5H, and S6H). Using spheroids derived from the TUBA1B-mEGFP hiPS cell line, we noticed that by 12 daf hSpS sent out abundant projections to the 3D hSkM (Figure 5I). To verify the specificity of these projections, we next performed retrograde rabies tracing. We delivered the ΔG-rabies-Cre-eGFP virus together with an AAV-G to differentiated hSkM that were assembled with day 37 hSpS (Figure 5J). We examined expression of GFP in hSpS 18 days after assembly and found that 90% of $GFP^+$ cells were $CHAT^+$, while less than 5% of these cells were $GABA^+$ (Figures 5K, 5L, S6I, and S6J). Further quantification showed that ~45% of these cells were also positive for the motor neuron-related transcription factor ISL1 but not for CHX10, PROX1, or FOXP2 (Figures S6K–S6M).

Next, we investigated whether hSpS cholinergic projections were functionally connected to hSkM using glutamate uncaging. We used 405 nm photostimulation in the presence of MNI-caged glutamate in the medium to rapidly and locally release glutamate (Figure S6N; Table S1 includes details of all stimulation experiments). Photostimulation of hSpS in hSpS-hSkM assembloids resulted in robust hSkM contraction in the presence, but not in the absence, of MNI-caged glutamate (Figures 5M, 5N, S6O, and S6P; Video S3), and addition of curare stopped hSkM contractions (100 μM; Figure 5N). Last, we used immunocytochemistry to verify the presence of neuromuscular junctions by labeling $Desmin^+$ myofibers with the pre-synaptic marker synaptophysin and BTX (Figures 5O and S6Q–S6S).

## Functional Applications in Cortico-Motor Assembloids

To model higher-order control of motor output, we implemented the tools described above to generate and characterize a

(K and L) Representative immunocytochemistry image for CTIP2 (K) or BRN2 (L) on the hCS side of hCS-hSpS assembloids at 31 daf.
(M) Quantification of the percentage (%) of $GFP^+$ and $mCherry^+$ cells on the hCS side that co-express either CTIP2 or BRN2 (n = 10 assembloids derived from 3 hiPS cell lines from 1–2 separate differentiations, with 2–3 cryosections quantified per assembloid).
(N) Quantification of the percentage (%) of $CTIP2^+$ or $BRN2^+$ among all $Hoechst^+$ cells in hCS (n = 6 assembloids derived from 3 hiPS cell lines from 1–2 separate differentiations, with 2–3 cryosections quantified per assembloid).
Data represent mean ± SEM unless otherwise specified. Scale bars, 50 μm (C, H, I, K, L, and inset in I), 100 μm (F), and 200 μm (B).
See also Figure S5 and Table S1.

Please cite this article in press as: Andersen et al., Generation of Functional Human 3D Cortico-Motor Assembloids, Cell (2020), https://doi.org/10.1016/j.cell.2020.11.017



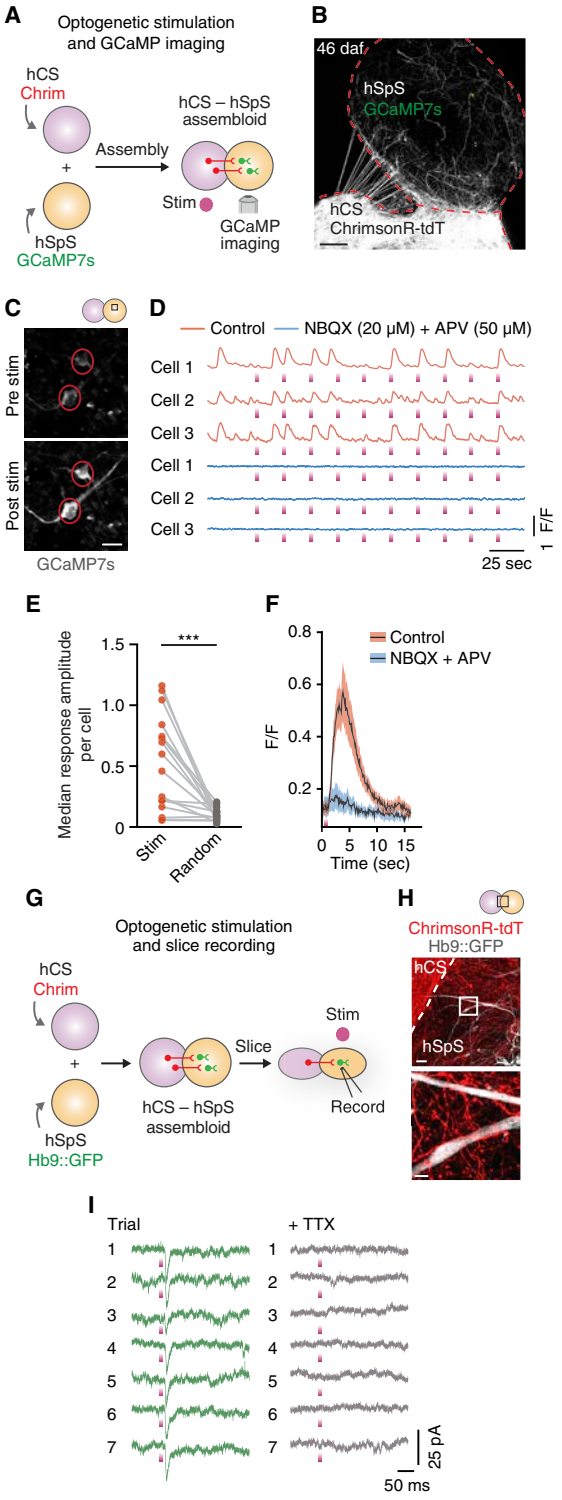


**Figure 4. Functional Connectivity in hCS-hSpS Assembloids**

(A) Schematic detailing optogenetic stimulation coupled with GCaMP imaging in hCS-hSpS assembloids.

(B) Representative picture of intact hCS$^{AAV\text{-}Chrim}$-hSpS$^{GCaMP7s}$ assembloid 46 days after fusion (daf).

functional cortico-motor unit *in vitro*. We fused intact hCS with hSpS and 3D hSkM on top of transwell inserts (Figures 6A and 6B). We then verified the presence of spontaneous contractions in hSkM. We looked at displacement of pixels over time in imaging fields (subdivided into 16 subfields; Figure S7A). We found that hSpS-hSkM and hCS-hSpS-hSkM assembloids displayed ~5× more spontaneous contractions compared to hSkM alone or hCS-hSkM assembloids ($p = 0.03$ for hSpS-hSkM versus hSkM; $p = 0.0003$ for hCS-hSpS-hSkM versus hSkM) (Figure 6C; Video S4). Moreover, we found that spontaneous activity in hSpS-hSkM and hCS-hSpS-hSkM assembloids was more coordinated across fields as assessed by analysis of the covariance between subfields in an imaging field ($p = 0.01$ for hSpS-hSkM versus hSkM, $p = 0.03$ for hCS-hSpS-hSkM versus hSkM) (Figures 6D, 6E, S7B, and S7C). However, we found no significant difference in the number of contractions or the covariance between hSpS-hSkM and hCS-hSpS-hSkM ($p = >0.99$).

Next, we probed the functional connectivity by selective stimulation of hCS. We used glutamate uncaging to photostimulate hCS in hCS-hSpS-hSkM assembloids (405 nm, 340 ms). This resulted in robust muscle contraction ($p = 0.002$) (Figures 6F–6H) suggesting functional assembly of a cortico-spinal-muscle functional unit. The contraction was blocked by treatment with 100 μm curare (Figures 6G, S7D, and S7E) and was not related to UV exposure (Figures S7F and S7G). Moreover, glutamate uncaging of hCS in hCS-hSkM did not elicit a response (Figures 6I and 6J), showing that muscle contraction upon cortical stimulation is dependent on the presence of the hSpS.

To validate cortical activation of muscle in hCS-hSpS-hSkM assembloids and achieve broader stimulation, we used optogenetics. We delivered Chrimson into hCS before assembly (Figures 6K and S7H) and used light stimulation (68 ms at 625 nm, 5 pulses, 100 frames or 6.8 s apart each) at 20–30 days after hCS-hSpS-hSkM assembly. Activation of Chrimson-expressing hCS induced global contractions in hSkM in 85.7% of tested assembloids ($p = 0.01$) (Figures 6L and 6M; Video S5, sequence 1) and 40% of pulses (Figure 6N shows the distribution of

(C) Representative images of two GCaMP7s-infected cells in an hCS-hSpS assembloid before and after optogenetic stimulation (625 nm, 100 ms each).

(D) Representative ΔF/F traces showing spontaneous and light-evoked calcium responses in three GCaMP7s-infected cells before and after adding NBQX (20 μM) and APV (50 μM). Optogenetic stimulation (625 nm, 100 ms each) is indicated with a purple rectangle. ΔF/F indicates the fluorescence intensity over baseline fluorescence.

(E) Quantification of the stimulation-triggered ΔF/F amplitudes, shown in comparison to randomized-triggered amplitudes (n = 16 cells from 4 assembloids derived from 2 hiPS cell lines from 1–2 differentiations; two-tailed paired t test: ***$p = 0.0005$).

(F) Stimulation-triggered average of the calcium response to optogenetic stimulation in paired cells with and without NBQX and APV (n = 16 cells from 4 assembloids derived from 2 hiPS cell lines). Black traces represent the mean and shaded bars represent the SEM.

(G) Schematic detailing optogenetic stimulation coupled with patch clamping slice recording in hCS-hSpS assembloids.

(H) Example images of an hCS$^{AAV\text{-}Chrim}$-hSpS$^{Hb9::GFP}$ assembloid.

(I) Chrimson-triggered EPSCs in an Hb9::GFP$^{+}$ neuron voltage clamped to –70 mV, (left) and lack of EPSCs following TTX application (right).

Scale bars, 10 μm (inset in H), 20 μm (C), 50 μm (H), and 200 μm (B).

See also Table S1.

Please cite this article in press as: Andersen et al., Generation of Functional Human 3D Cortico-Motor Assembloids, Cell (2020), https://doi.org/10.1016/j.cell.2020.11.017



CellPress

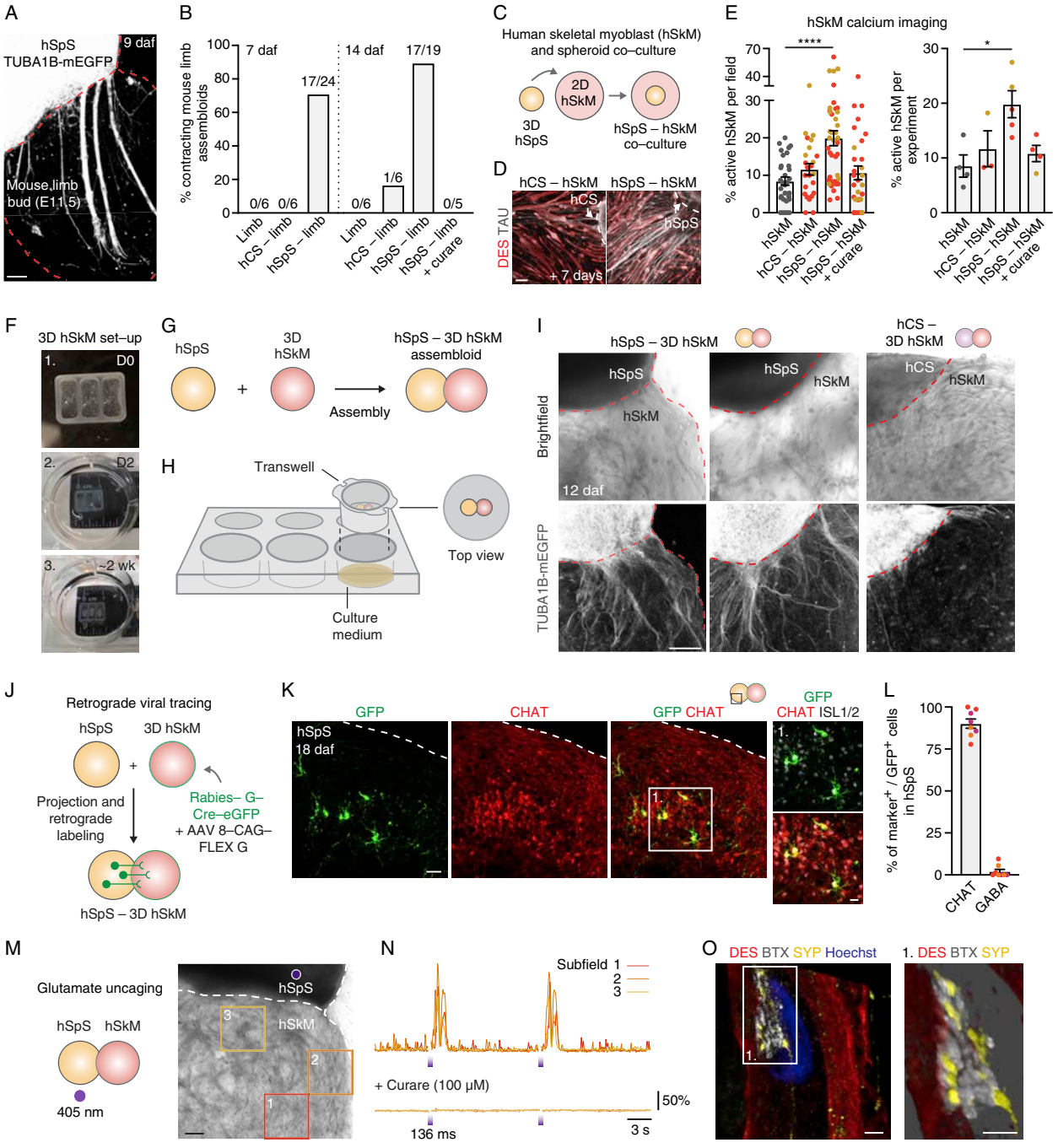


**Figure 5. hSpS Control of Muscle Activity**

(A) Image of intact assembloid showing hSpS derived from TUBA1B-mEGFP projecting into mouse limb. This image was generated by manual stitching of individual images.

(B) Quantification of the proportion of contracting limb, hCS-limb or hSpS-limb assembloids 7 and 14 days after fusion (daf; n = 3 hiPS cell lines from 1 differentiation; $\chi^2$ test, p = 0.02), in the absence or presence of curare (100 µM; n = 3 hiPS cell lines; $\chi^2$ test, p = 0.02). See Video S2, sequence 1, for live imaging of a contracting hSpS-limb assembloid with or without curare.

(C) Schematic showing the co-culture of 2D human skeletal myoblasts (hSkM) and spheroids (hCS or hSpS).

(D) Immunocytochemistry of 2D hSkM 7 days after co-culture with hCS or hSpS.

(E) Quantification of spontaneous calcium activity in hSkM (Cal-590 AM) in either hSkM alone or after co-culture with hCS, hSpS or hSpS + curare (100 µM). Graph on the left shows % of active hSkM per field recorded (n = 2 hiPS cell lines from 1–2 differentiations; Kruskal-Wallis test: p < 0.0001, with Dunn's multiple

*(legend continued on next page)*

Please cite this article in press as: Andersen et al., Generation of Functional Human 3D Cortico-Motor Assembloids, Cell (2020), https://doi.org/10.1016/j.cell.2020.11.017



successful stimulation and Figures S7I and S7J show an example where muscle contraction is induced in only 2 of the 5 light pulses; Table S1), while stimulation of Chrimson-expressing hCS in hCS-hSkM did not trigger a response (Figures S7K and S7L). To test whether this response was mediated by glutamatergic transmission, we added the AMPA and NMDA receptor blockers NBQX (50 μM) and APV (50 μM), which completely abolished light-induced responses (Figures 6M and 6O).

Next, to test whether hCS-hSpS-hSkM assembloids could be entirely derived from hiPS cells, we generated hiPS cell-derived skeletal myoblasts using a protocol adapted from Chal et al. (2016) (Figure S8A). Following myoblast differentiation, subculturing and fluorescence-activated cell sorting (FACS) purification (Figures S8B–S8F), we generated 3D hiPS cell-derived hSkM (ihSkM) as we did for primary myoblasts in Figure 5F. We found that these 3D ihSkM can also be assembled with hSpS and hCS to generate three-part assembloids (Figure S8G) that display contraction following optogenetic stimulation (Figures S8H and S8I).

Because quantification of contractions and displacement depends on changes in pixel intensities, and this could vary from preparation to preparation and over time, we next implemented the use of a calcium indicator expressed under a muscle-specific promoter to monitor cellular activity in hSkM. For this, we delivered Chrimson into hCS as well as lenti-ACTA1::GCaMP6s into hSkM, and used light stimulation (100 ms at 625 nm, 5 pulses, 100 frames or 10 s apart each) at 4 weeks after hCS-hSpS-hSkM assembly (Figure 6P). Activation of Chrim-expressing hCS induced calcium spikes in hSkM fibers (Figures 6Q and 6R; Video S5, sequence 2), and these were dependent on the presence of Chrimson, as light stimulation of hCS-hSpS-hSkM assembloids in the absence of the opsin did not elicit any responses (Figures 6S and 6T).

## Long-Term Culture and Functionality of Cortico-Motor Assembloids

Conventional motor neuron and muscle co-cultures are not amenable to long-term experiments, as cells tend to detach over time (Thomson et al., 2012). We found that hCS-hSpS-hSkM can be kept in culture for up to 10 weeks post-assembly (~16–18 weeks from the initiation of hSpS differentiation). To characterize cortico-motor assembloids over time, we first performed electron microscopy 8 weeks after assembly (Figures 7A–7F and S7M–S7S). We found that assembloids at this time present intact axons and dendrites (Figure S7N), mature synapses (Figures 7B, 7C, S7O, and S7P), organized skeletal muscle fibers (Figures 7D and S7Q), and neuromuscular contacts (Figures 7E, 7F, S7R, and S7S). Moreover, we used immunohistochemistry in hCS-hSpS-hSkM assembloids at 10 weeks (Figure 7G) and found the presence of hCS-derived projections into hSpS (Figures 7H and S7U), motor neurons (Figure 7I, S7U, and S7V), non-reactive astrocytes (Figures 7H and S7V), myelinating oligodendrocytes (Figures 7H and 7I) and neuromuscular junctions (Figure 7J). Together, these data indicate that hCS-hSpS-hSkM assembloids can be maintained in culture for up to 10 weeks without structural disintegration.

Next, we probed the ability of hCS-hSpS-hSkM assembloids to maintain functional connections over 8 weeks post-assembly. For this, we generated $hCS^{AAV\text{-}Chrim}$-hSpS-hSkM assembloids and performed optogenetic stimulations at 5 and 8 weeks (Figure 7K). We found that hSkM contracted after light stimulation at both time points, although the success rate for contracting assembloids at 8 weeks tended to be decreased (50% versus 81% success rate at 8 and 5 weeks, respectively; $p = 0.06$; Figure 7L). Interestingly, however, assembloids at 8 weeks tended to be more likely to repeatedly contract following five consecutive stimulations (Figures 7M and 7N; $p = 0.06$), suggesting a more robust response after long-term culture. To investigate this further, we imaged calcium activity using GCaMP6s in hSkM fibers following optogenetic stimulation at 4–5 or at 7–8 weeks (Figure 7O). Light-induced hCS activity elicited calcium spikes in hSkM at both 4–5 and 7–8 weeks, but although hSkM fibers in assembloids respond to the first stimulation at both ages, only at the later time point cells are able to maintain a robust response after 5 stimulations (Figures 7P and 7Q; $p = 0.003$ for Stim 5).

Taken together, these results demonstrate that the assembly of intact 3D human cultures resembling the cerebral cortex, hindbrain/spinal cord and skeletal muscle enables the formation of neural circuits that can be readily manipulated over several weeks *in vitro* to model cortical control of muscle contraction.

comparison test ****$p < 0.0001$). Graph on the right shows the percentage (%) of active hSkM per co-culture experiment (fields imaged in one experiment combined; n = 2 hiPS cell lines from 1–2 differentiations; Kruskal-Wallis test: $p = 0.02$, with Dunn's multiple comparison test *$p = 0.01$). See Video S2, sequence 2 for calcium activity of hSkM and hSpS-hSkM.

(F) Images showing the generation of 3D hSkM and the assembly with hCS and hSpS. (1) Dissociated hSkM are resuspended in Geltrex and placed in silicone wells. (2) Silicone wells are placed in ultra-low attachment plates in hSkM growth medium. (3) hSkM growth medium is switched to differentiation medium.

(G and H) Schematics showing hSpS-hSkM assembloid set-up.

(I) Representative images of 3D hSkM that have been assembled with hCS or hSpS derived from a TUBA1B-mEGFP hiPS cell line.

(J) Schematic detailing retrograde viral tracing experiment in hSpS-hSkM assembloid.

(K) Representative immunohistochemistry image for rabies-derived GFP, CHAT, and ISL1 on the hSpS side of hSpS-hSkM assembloids at 18 daf.

(L) Quantification of the percentage (%) of $GFP^+$ cells on the hSpS side of hSpS-hSkM assembloids that co-express either CHAT or GABA (n = 8 assembloids derived from 3 hiPS cell lines from 1 differentiation, with 3–6 cryosections quantified per assembloid).

(M and N) Glutamate uncaging in hSpS-hSkM assembloid. UV light (405 nm, 136 ms) uncages glutamate on hSpS (M). Displacement normalized to baseline over time is shown for 3 subfields in the presence or absence of curare (100 μM; N). See Video S3 for an example of glutamate uncaging in an hSpS-hSkM assembloid. Table S1 shows details of all stimulation experiments.

(O) Representative immunohistochemistry showing a neuromuscular junction (NMJ) with synaptophysin 1 (SYP) and bungarotoxin (BTX) on a $desmin^+$ (DES) myofiber. Inset: 3D rendering of the NMJ.

Data represent mean ± SEM. Scale bars, 2 μm (O), 20 μm (inset in K), 50 μm (K), 100 μm (A), and 200 μm (D, I, and M).

See also Figure S6.

Please cite this article in press as: Andersen et al., Generation of Functional Human 3D Cortico-Motor Assembloids, Cell (2020), https://doi.org/10.1016/j.cell.2020.11.017



CellPress

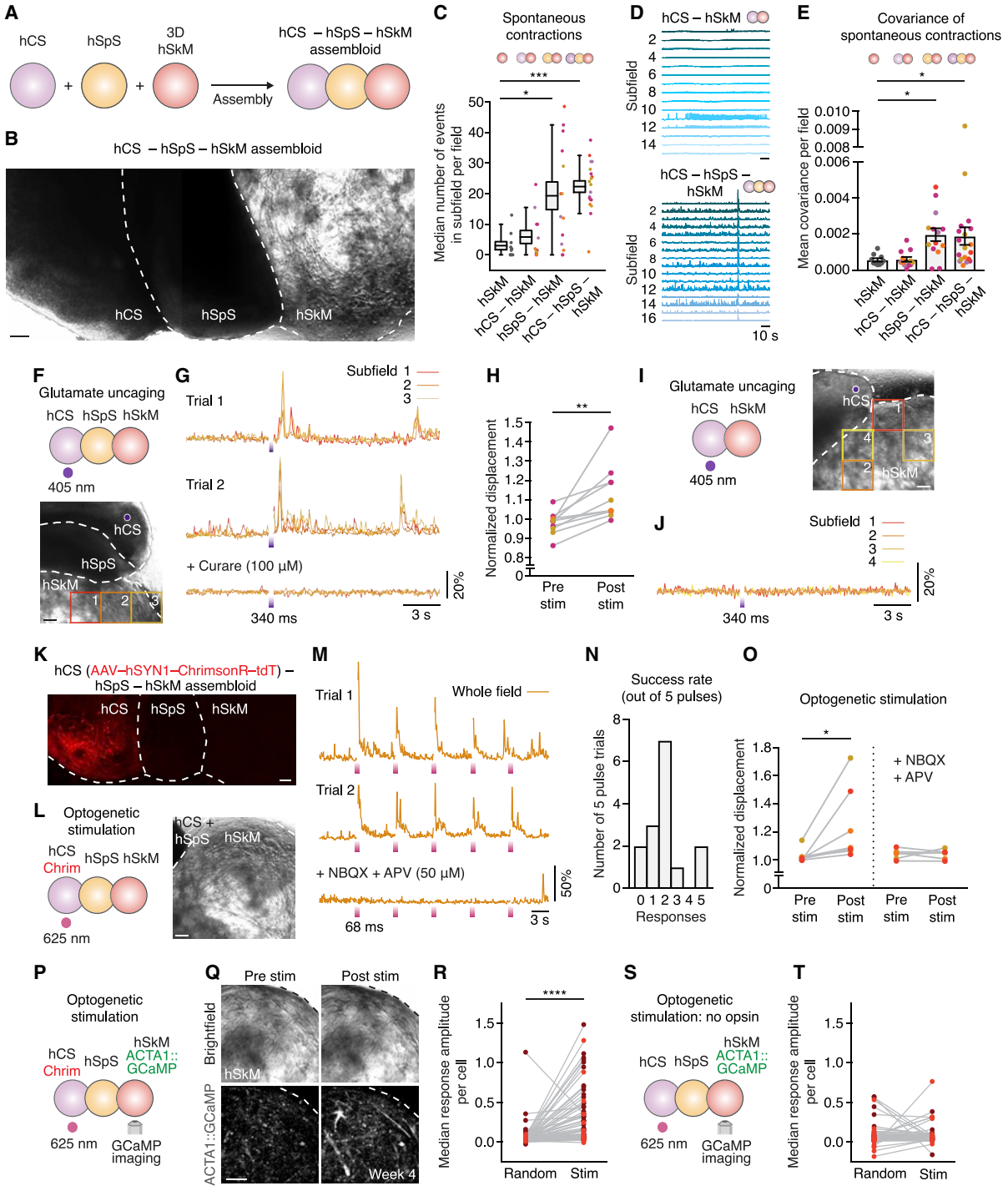


**Figure 6. Cortical Activity Modulates Muscle Function in hCS-hSpS-hSkM Assembloids**

(A) Schematic showing hCS-hSpS-hSkM assembloid set-up.

(B) Representative image showing intact hCS-hSpS-hSkM assembloid. This image was generated by manual stitching of individual images.

(C) Quantification of spontaneous contractions over a 2-min period showing the median number of events in subfields per field (n = 10 fields from 5 assembloids for hSkM, n = 12 fields from 6 assembloids from 1–2 differentiations for hCS-hSkM, n = 14 fields from 7 assembloids from 1–2 differentiations for hSpS-hSkM, n = 19 fields from 11 assembloids from 1–2 differentiations for hCS-hSpS-hSkM; Kruskal-Wallis test $p < 0.0001$, with Dunn's multiple comparison test: *p = 0.03 for

(legend continued on next page)

Please cite this article in press as: Andersen et al., Generation of Functional Human 3D Cortico-Motor Assembloids, Cell (2020), https://doi.org/10.1016/j.cell.2020.11.017



## DISCUSSION

Cell reprograming and the subsequent derivation of human neurons from patients holds great promise for studying brain disorders (Amin and Paşca, 2018; Dolmetsch and Geschwind, 2011; Han et al., 2011). However, modeling of complex cell-cell interactions and circuit assembly *in vitro* remains a challenge (Paşca, 2018, 2019). We previously showed the potential of using region-specific spheroids as a modular approach to study human interneuron migration and identify disease phenotypes (Birey et al., 2017). Here, we leveraged this approach to generate an intact, three-component cortico-motor circuit in which cortical neural activation controls muscle contraction via activation of motor neurons. This represents a significant advance beyond prior models in which individual components of motor circuits have been generated in 3D in isolation or co-cultured in 2D (Duval et al., 2019; Ogura et al., 2018; Sances et al., 2016; Shi et al., 2018; Steinbeck et al., 2016). First, we used human-derived components that are assembled in a self-organizing 3D preparation, and we achieved this reliably using multiple hiPS cells lines. Second, we built assembloids from intact, 3D cultures that have been patterned to resemble specific regions of the central nervous system. Specifically, we have generated hSpS that contain a large diversity of spinal neuronal domains and shown they resemble *in vivo* neuronal populations in mouse. This allows greater cell diversity while leveraging the ability of specific neural populations to form human circuits. Third, we showed the generation, from three components, of a functional human neural circuit that contains at least two synaptic contacts. Moreover, we implemented a series of neuroscience tools and showed that this system can be used for tracing connectivity using a rabies virus, as well as for probing and manipulating neural activity using calcium imaging, glutamate uncaging, and optogenetic stimulation. Finally, we showed that this three-part assembloid can be maintained functionally and morphologically intact for up to 10 weeks *in vitro*. This feature may allow for further refinement and maturation of connections, as well as myelination, which could facilitate the study of cellular phenotypes of neurodegenerative disorders.

Moving forward, there are a number of potential applications for this cellular platform that could be used to gain insights into the evolution, development, and disorders of the cortico-spinal-muscle circuit. For instance, primates possess direct monosynaptic cortico-spinal connections that control fine motor movements (Lemon, 2008; Sousa et al., 2017), and a better understanding of the underlying developmental mechanisms of

hSpS-hSkM versus hSkM, ***p = 0.0003 for hCS-hSpS-hSkM versus hSkM). Boxplot shows mean ± SEM and whiskers show 90$^{th}$ and 10$^{th}$ percentiles. See Video S4 for an example of spontaneous contractions in an hCS-hSpS-hSkM assembloid.

(D) Representative spontaneous contraction traces in subfields of hCS-hSkM or hCS-hSpS-hSkM assembloids.

(E) Correlation of displacements between subfields in a field quantified using covariance analysis. Data represent mean ± SEM (n = 10 fields from 5 assembloids for hSkM, n = 12 fields from 6 assembloids for hCS-hSkM, n = 14 fields from 7 assembloids for hSpS-hSkM, n = 19 fields from 11 assembloids for hCS-hSpS-hSkM; Kruskal-Wallis test p = 0.001, with Dunn's multiple comparison test: *p = 0.01 for hSpS-hSkM versus hSkM, *p = 0.03 for hCS-hSpS-hSkM versus hSkM).

(F and G) Glutamate uncaging in hCS-hSpS-hSkM assembloid. UV light (405 nm) uncages glutamate specifically on hCS (F). Displacement normalized to baseline over time is shown for 3 subfields and two trials (G).

(H) Quantification of displacement normalized to baseline in different glutamate uncaging experiments. Values of the last frame before stimulation (Pre stim) and the highest of the first 3 frames or 204 ms after stimulation (Post stim) are plotted per field (subfields per field are averaged; n = 10 fields from 7 assembloids derived from 3 hiPS cell lines from 1–2 differentiations; Wilcoxon test **p = 0.002).

(I and J) Glutamate uncaging of hCS in hCS-hSkM assembloid (I). Displacement normalized to baseline over time is shown for 4 subfields in the presence of caged glutamate (J). Similar results were obtained in n = 4 hCS-hSkM assembloids derived from 2 hiPS cell lines.

(K) Representative image showing an intact hCS-hSpS-hSkM assembloid in which hCS was infected with AAV-hSYN1-ChrimsonR-tdT prior to assembly. This image was generated by manual stitching of individual images.

(L and M) Optogenetic stimulation in hCS-hSpS-hSkM assembloids. Five consecutive pulses of light (625 nm, 68 ms in duration each and 6.8 s apart) were delivered (L). Traces of whole-field muscle displacement are shown after normalization to the pre-stimulation baseline in the absence or presence of NBQX (50 μM) and APV (50 μM) (M). See Video S5, sequence 1 for an example of optogenetic stimulation in a hCS-hSpS-hSkM assembloid.

(N) Histogram illustrating the success rate of optogenetic stimulation (out of 5 consecutive pulses for each assembloid; n = 15 trials of 5 pulses in 7 assembloids from 1–2 differentiations).

(O) Quantification of displacement (normalized to pre-stimulation baseline) per assembloid in the presence or absence of NBQX and APV (50 μM). Pre stim represents the highest value of displacement in the 20 frames (1.36 s) before stimulation. Post stim represents the average across 5 pulses of the highest value in the 20 frames immediately following stimulation (left: n = 7 assembloids derived from 3 hiPS cell lines from 1–2 differentiations; Wilcoxon matched paired t test *p = 0.01; right: n = 6 assembloids derived from 3 hiPS cell lines from 1–2 differentiations; two-tailed paired t test p = 0.94). Table S1 includes details of stimulation experiments.

(P) Optogenetic stimulation coupled with calcium imaging in hCS$^{AAV\text{-}Chrim}$-hSpS-hSkM$^{ACTA1::GCaMP6s}$. Five consecutive pulses of light (625 nm, 100 ms in duration each and 10 s apart) were delivered.

(Q) Representative bright-field and ACTA1::GCaMP6s images of hSkM in hCS-hSpS-hSkM assembloid before and after stimulation. See Video S5, sequence 2 for an example of optogenetic stimulation coupled with calcium imaging in a hCS-hSpS-hSkM assembloid.

(R) Quantification of the stimulation-triggered ΔF/F amplitudes, shown in comparison to randomized-triggered amplitudes in hSkM cells. The median ΔF/F amplitude of the five pulses delivered per cell is shown (n = 82 cells from 8 fields in 6 assembloids derived from 2 hiPS cell lines and 2 separate differentiations; Wilcoxon matched paired t test: ****p < 0.0001).

(S) Optogenetic stimulation in hCS-hSpS-hSkM$^{ACTA1::GCaMP6s}$ assembloid (no opsin; five consecutive 100-ms pulses).

(T) Quantification of stimulation-triggered ΔF/F amplitudes, shown in comparison to randomized-triggered amplitudes in hSkM cells of hCS-hSpS-hSkM assembloids without Chrimson. The median ΔF/F amplitudes of the five pulses delivered per cell are shown (n = 91 cells from 6 fields in 4 assembloids derived from 2 hiPS cell lines and 1 differentiation; Wilcoxon matched paired t test: p = 0.27).

Scale bars, 200 μm (B, F, I, K, L, and Q).

See also Figures S7 and S8.

Please cite this article in press as: Andersen et al., Generation of Functional Human 3D Cortico-Motor Assembloids, Cell (2020), https://doi.org/10.1016/j.cell.2020.11.017



CellPress

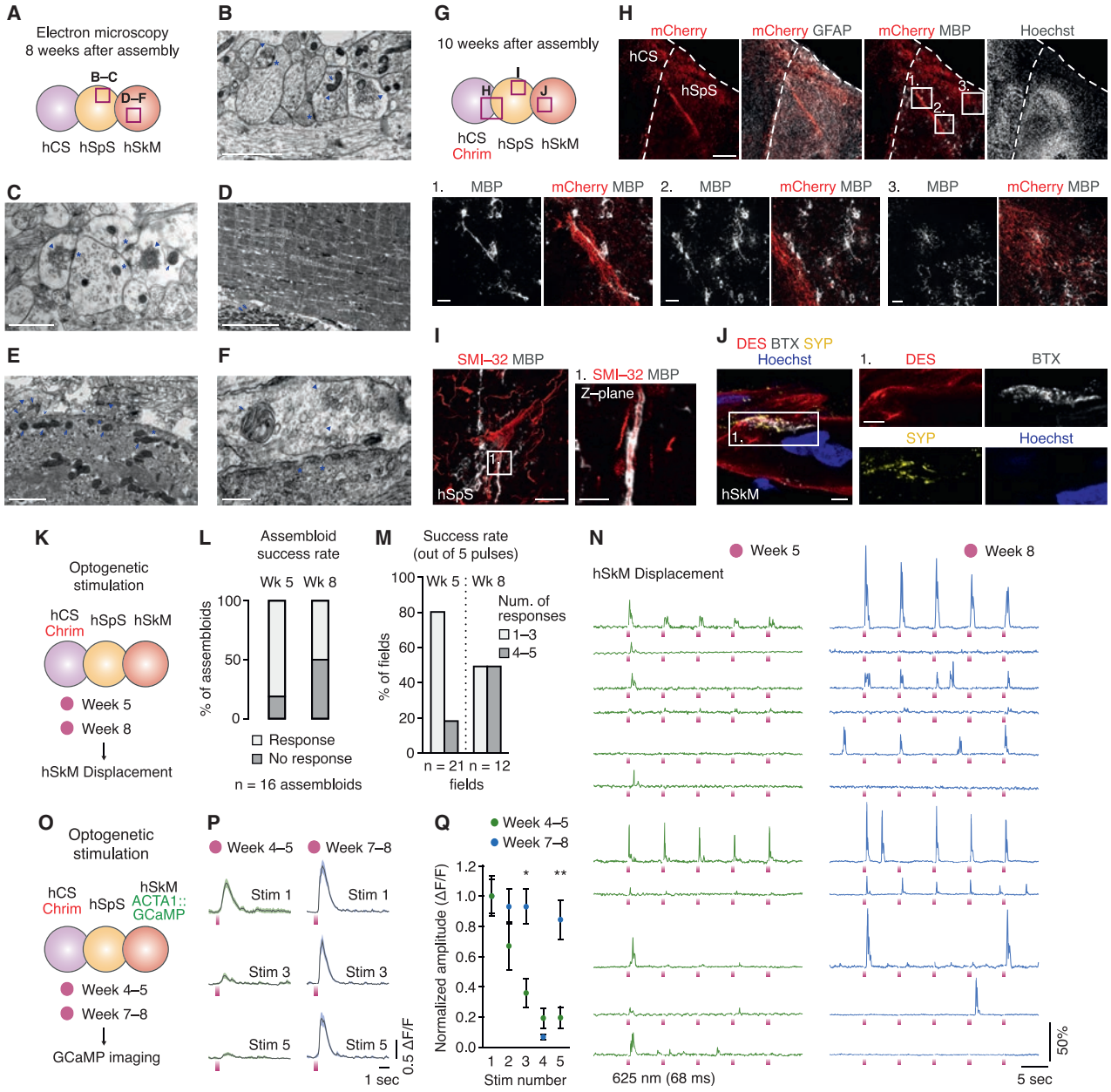


**Figure 7. Long-Term Culture and Functionality of hCS-hSpS-hSkM Assembloids**

(A) Schematic detailing location of electron microscopy images within hCS-hSpS-hSkM assembloids.

(B and C) Representative images within hSpS in hCS-hSpS-hSkM assembloids showing dendrites and synapses with synaptic vesicles (arrowheads), post-synaptic densities (asterisks), and mitochondria (arrows).

(D) Representative images within hSkM in hCS-hSpS-hSkM assembloids showing skeletal muscle fibers with actin and myosin filaments and mitochondria (arrows).

(E and F) Representative images within hSkM in hCS-hSpS-hSkM assembloids showing points of contact between hSpS neurons and hSkM. Neuron terminals are vesicle-laden (arrow heads) and present mitochondria (arrows). hSkM are surrounded by a basal lamina (hollow arrowheads) and present small invaginations on the membrane (asterisks, F).

(G) Schematic detailing location of images within hCS$^{AAV\text{-}Chrim}$-hSpS-hSkM assembloids.

(H–J) Representative immunohistochemistry images in cryosections of hCS$^{AAV\text{-}Chrim}$-hSpS-hSkM assembloids showing oligodendrocytes (H), motor neurons (I) and neuromuscular junctions (J). Insets in (H) show oligodendrocytes in hSpS, and inset in (I) shows a single Z plane.

(K) Optogenetic stimulation in hCS-hSpS-hSkM assembloid (five consecutive 68 ms pulses) at 5 and 8 weeks post-assembly. Displacement in hSkM was quantified.

*(legend continued on next page)*

Please cite this article in press as: Andersen et al., Generation of Functional Human 3D Cortico-Motor Assembloids, Cell (2020), https://doi.org/10.1016/j.cell.2020.11.017



assembly could bring insights into the unique primate aspects of this circuit. Moreover, patient-derived cells could be used to dissect cell-autonomous effects and cell-specific vulnerabilities in the context of amyotrophic lateral sclerosis or spinal muscular atrophy (Garden and La Spada, 2012). Co-culture with autologous immune cells may reveal the cellular cross-talk underlying multiple sclerosis and other autoimmune conditions. We also envision that, once assembled, this three-way system could be physically perturbed at various levels (cortical, hindbrain-cervical) to develop a human cellular model of spinal cord injury (SCI) (Thiry et al., 2020) and to investigate regeneration at early stages of development. In the context of SCI, these studies could also explore damage affecting the phrenic nerve that controls the thin diaphragmatic skeletal muscle. In addition, assembly with other brain regions such as dorsal root ganglia neurons or midbrain spheroids, could be used to model sensory input (Koch et al., 2018; Levine et al., 2012) or rubrospinal tract connectivity (Cregg et al., 2020). Ultimately, assembloids of various parts of the CNS could bring insights into understanding assembly of different types of human circuits and into identifying therapeutic strategies.

### Limitations of Study

These applications would greatly benefit from further improvements such as the generation of more caudal spinal cord cell types (Faustino Martins et al., 2020; Gouti et al., 2014), the presence of organizing centers or implementation of other strategies to improve progenitor domain organization as illustrated by Duval et al. (2019) and Ogura et al. (2018), and the assessment of ascending projections. Moreover, further optimization of optogenetic approaches with cell-type-specific reporters could better capture connectivity.

## STAR★METHODS

Detailed methods are provided in the online version of this paper and include the following:

- KEY RESOURCES TABLE
- RESOURCE AVAILABILITY
  - Lead Contact
  - Materials Availability
  - Data and Code availability
- EXPERIMENTAL MODEL AND SUBJECT DETAILS
  - Culture of hiPS cells
  - Human primary brain tissue
- METHOD DETAILS
  - Variability terminology
  - Generation of hCS and hSpS from hiPS cells
  - Generation of CAG::EGFP hiPS cell line
  - Generation of hCS-hSpS assembloids
  - Culture of hSkM
  - Generation of 3D hSkM
  - Generation of ihSkM and 3D ihSkM
  - Generation of hSpS-hSkM and hCS-hSpS-hSkM
  - Co-culture of mouse limb and spheroids
  - Viral labeling and rabies-ΔG tracing
  - Projection imaging in intact hCS-hSpS
  - hSkM Cal-590 calcium imaging
  - Optogenetics and GCaMP imaging in hCS-hSpS
  - Glutamate uncaging and optogenetics in hCS-hSpS-hSkM
  - Cryopreservation and immunohistochemistry
  - Transmission electron microscopy
  - Real-time quantitative PCR - qPCR
  - Single cell dissociation
  - Single cell gene expression - BD Rhapsody
  - Single cell gene expression - 10x Genomics
  - Electrophysiology
- QUANTIFICATION AND STATISTICAL ANALYSIS
  - Fluorescence intensity quantification
  - Projection quantification
  - hSkM Cal-590 calcium imaging
  - hSkM GCaMP6s analysis
  - GCaMP7s analysis
  - Contraction analysis

## SUPPLEMENTAL INFORMATION

Supplemental Information can be found online at https://doi.org/10.1016/j.cell.2020.11.017.

## ACKNOWLEDGMENTS

We thank K.M. Hennig, S.J. Yoon, M.L. Fabian, F. Birey, R.M. Agoglia, M. Li, A.E. Trevino, and the Paşca lab for advice and support. We also thank J. Perrino (Stanford Cell Sciences Imaging Facility) for support with electron microscopy. Cell sorting was performed in the Stanford Shared FACS Facility. The rabies virus work was supported by the GT3 Core Facility of the Salk Institute

(L) Success rate per assembloid following optogenetic stimulation at 5 and 8 weeks post-assembly. Two separate fields per assembloid were imaged at each time-point (n = 16 assembloids for both time-points from 2 hiPS cell lines and 1 differentiation; $\chi^2$ test, p = 0.06).
(M) Success rate out of 5 consecutive light pulses per responding field following optogenetic stimulation at 5 and 8 weeks post-assembly (n = 21 and 12 fields for weeks 5 and 8, respectively, from 13 or 8 assembloids derived from 2 hiPS cell lines and 1 differentiation; $\chi^2$ test, p = 0.06).
(N) Representative traces of whole-field muscle displacement shown after normalization to the pre-stimulation baseline in hCS-hSpS-hSkM assembloid (five consecutive 68-ms pulses) at 5 and 8 weeks post-assembly.
(O) Optogenetic stimulation coupled with calcium imaging in $hCS^{AAV\text{-}Chrim}$-hSpS-$hSkM^{ACTA1::GCaMP6s}$ at 4–5 and 7–8 weeks post-assembly. Five consecutive pulses of light (625 nm, 100 ms in duration each and 10 s apart) were delivered.
(P) Average ACTA1::GCaMP6s signal aligned to the time of the pulse in stimulations of numbers 1, 3, and 5 in hCS-hSpS-hSkM assembloids at 4–5 and 7–8 weeks after assembly.
(Q) GCaMP6s ΔF/F amplitudes plotted for stimulation numbers 1–5 normalized to the first stimulation (n = 22 cells from 4 assembloids from 1 differentiation at 4–5 weeks, and 13 cells from 3 assembloids from 1 differentiation at 7–8 weeks; two-way repeated-measures ANOVA with Tukey multiple comparisons: *p = 0.1, **p = 0.003).
Scale bars, 200 nm (F), 1 μm (C and E), 2 μm (B), 5 μm (D, J, and inset in I), 20 μm (I and insets in H), and 200 μm (H).

with funding from NIH NCI CCSG P30 014195, an NINDS R24 Core Grant, and funding from NEI. Electron microscopy work was supported, in part, by ARRA Award Number 1S10RR026780-01 from the National Center for Research Resources (NCRR). This work was supported by grants from National Institute of Mental Health (NIMH) (BRAINS Award R01MH107800), the Chan Zuckerberg Initiative Ben Barres Investigator Award, the NYSCF Robertson Stem Cell Investigator Award, the Stanford Brain Organogenesis Progam in the Wu Tsai Neurosciences Institute and the Big Idea Grant, Stanford Bio-X, the Kwan Research Fund, V. Coates Foundation, the Senkut Funds (to S.P.P.), the Idun Berry Postdoctoral Fellowship (to J.A.), the Stanford Medicine Dean's Fellowship (to J.A. and Y.M.), and the Stanford Maternal & Child Health Research Institute (MCHRI) Fellowship (to O.R. and Y.M.).

## AUTHOR CONTRIBUTIONS

J.A. developed the differentiation and assembly method and performed experiments. O.R. conducted and analyzed electrophysiology experiments and contributed to developing the analysis pipelines. Y.M. contributed to the retrograde viral tracing experiments. M.S. contributed to the myoblast differentiation experiments. X.C. generated the fluorescently labeled hiPS cell line and performed FACS experiments. H.V. contributed to the ultrastructural characterization of assembloids. E.M.W., H.C.F., N.T., K.W.K., and N.D.A. performed the single cell transcriptomics experiments or analysis. N.T. and M.V.T. contributed to quantification and analyses. J.A. and S.P.P. wrote the manuscript with input from all authors. S.P.P. supervised the work.

## DECLARATION OF INTERESTS

Stanford University has filed a provisional patent application that covers the generation and assembly of region-specific cortico-spinal-muscle spheroids. H.C.F. and E.M.W. were employees of BD Genomics during this study.

Received: November 12, 2019
Revised: May 27, 2020
Accepted: November 4, 2020
Published: December 16, 2020

## REFERENCES

Alaynick, W.A., Jessell, T.M., and Pfaff, S.L. (2011). SnapShot: spinal cord development. Cell *146*, 178.

Amin, N.D., and Paşca, S.P. (2018). Building Models of Brain Disorders with Three-Dimensional Organoids. Neuron *100*, 389–405.

Amoroso, M.W., Croft, G.F., Williams, D.J., O'Keeffe, S., Carrasco, M.A., Davis, A.R., Roybon, L., Oakley, D.H., Maniatis, T., Henderson, C.E., and Wichterle, H. (2013). Accelerated high-yield generation of limb-innervating motor neurons from human stem cells. J. Neurosci. *33*, 574–586.

Birey, F., Andersen, J., Makinson, C.D., Islam, S., Wei, W., Huber, N., Fan, H.C., Metzler, K.R.C., Panagiotakos, G., Thom, N., et al. (2017). Assembly of functionally integrated human forebrain spheroids. Nature *545*, 54–59.

Blesch, A., and Tuszynski, M.H. (2009). Spinal cord injury: plasticity, regeneration and the challenge of translational drug development. Trends Neurosci. *32*, 41–47.

Borghese, L., Dolezalova, D., Opitz, T., Haupt, S., Leinhaas, A., Steinfarz, B., Koch, P., Edenhofer, F., Hampl, A., and Brüstle, O. (2010). Inhibition of notch signaling in human embryonic stem cell-derived neural stem cells delays G1/S phase transition and accelerates neuronal differentiation in vitro and in vivo. Stem Cells *28*, 955–964.

Brennan, K.J., and Hardeman, E.C. (1993). Quantitative analysis of the human alpha-skeletal actin gene in transgenic mice. J. Biol. Chem. *268*, 719–725.

Butler, A., Hoffman, P., Smibert, P., Papalexi, E., and Satija, R. (2018). Integrating single-cell transcriptomic data across different conditions, technologies, and species. Nat. Biotechnol. *36*, 411–420.

Butts, J.C., Iyer, N., White, N., Thompson, R., Sakiyama-Elbert, S., and McDevitt, T.C. (2019). V2a interneuron differentiation from mouse and human pluripotent stem cells. Nat. Protoc. *14*, 3033–3058.

Chal, J., Al Tanoury, Z., Hestin, M., Gobert, B., Aivio, S., Hick, A., Cherrier, T., Nesmith, A.P., Parker, K.K., and Pourquié, O. (2016). Generation of human muscle fibers and satellite-like cells from human pluripotent stem cells in vitro. Nat. Protoc. *11*, 1833–1850.

Coulon, P., Rollin, P.E., and Flamand, A. (1983). Molecular basis of rabies virus virulence. II. Identification of a site on the CVS glycoprotein associated with virulence. J. Gen. Virol. *64*, 693–696.

Cregg, J.M., Leiras, R., Montalant, A., Wanken, P., Wickersham, I.R., and Kiehn, O. (2020). Brainstem neurons that command mammalian locomotor asymmetries. Nat. Neurosci. *23*, 730–740.

Dasen, J.S., and Jessell, T.M. (2009). Hox networks and the origins of motor neuron diversity. Curr. Top. Dev. Biol. *88*, 169–200.

Delile, J., Rayon, T., Melchionda, M., Edwards, A., Briscoe, J., and Sagner, A. (2019). Single cell transcriptomics reveals spatial and temporal dynamics of gene expression in the developing mouse spinal cord. Development *146*, dev173807.

Dolmetsch, R., and Geschwind, D.H. (2011). The human brain in a dish: the promise of iPSC-derived neurons. Cell *145*, 831–834.

Duval, N., Vaslin, C., Barata, T.C., Frarma, Y., Contremoulins, V., Baudin, X., Nedelec, S., and Ribes, V.C. (2019). BMP4 patterns Smad activity and generates stereotyped cell fate organization in spinal organoids. Development *146*, dev175430.

Etessami, R., Conzelmann, K.K., Fadai-Ghotbi, B., Natelson, B., Tsiang, H., and Ceccaldi, P.E. (2000). Spread and pathogenic characteristics of a G-deficient rabies virus recombinant: an in vitro and in vivo study. J. Gen. Virol. *81*, 2147–2153.

Fan, H.C., Fu, G.K., and Fodor, S.P. (2015). Expression profiling. Combinatorial labeling of single cells for gene expression cytometry. Science *347*, 1258367.

Faustino Martins, J.M., Fischer, C., Urzi, A., Vidal, R., Kunz, S., Ruffault, P.L., Kabuss, L., Hube, I., Gazzerro, E., Birchmeier, C., et al. (2020). Self-Organizing 3D Human Trunk Neuromuscular Organoids. Cell Stem Cell *26*, 172–186.

Garden, G.A., and La Spada, A.R. (2012). Intercellular (mis)communication in neurodegenerative disease. Neuron *73*, 886–901.

Giandomenico, S.L., Mierau, S.B., Gibbons, G.M., Wenger, L.M.D., Masullo, L., Sit, T., Sutcliffe, M., Boulanger, J., Tripodi, M., Derivery, E., et al. (2019). Cerebral organoids at the air-liquid interface generate diverse nerve tracts with functional output. Nat. Neurosci. *22*, 669–679.

Goulding, M. (2009). Circuits controlling vertebrate locomotion: moving in a new direction. Nat. Rev. Neurosci. *10*, 507–518.

Gouti, M., Tsakiridis, A., Wymeersch, F.J., Huang, Y., Kleinjung, J., Wilson, V., and Briscoe, J. (2014). In vitro generation of neuromesodermal progenitors reveals distinct roles for wnt signalling in the specification of spinal cord and paraxial mesoderm identity. PLoS Biol. *12*, e1001937.

Greig, L.C., Woodworth, M.B., Galazo, M.J., Padmanabhan, H., and Macklis, J.D. (2013). Molecular logic of neocortical projection neuron specification, development and diversity. Nat. Rev. Neurosci. *14*, 755–769.

Gu, Z., Kalambogias, J., Yoshioka, S., Han, W., Li, Z., Kawasawa, Y.I., Pochareddy, S., Li, Z., Liu, F., Xu, X., et al. (2017). Control of species-dependent cortico-motoneuronal connections underlying manual dexterity. Science *357*, 400–404.

Guthrie, S. (2007). Patterning and axon guidance of cranial motor neurons. Nat. Rev. Neurosci. *8*, 859–871.

Han, S.S., Williams, L.A., and Eggan, K.C. (2011). Constructing and deconstructing stem cell models of neurological disease. Neuron *70*, 626–644.

Jessell, T.M. (2000). Neuronal specification in the spinal cord: inductive signals and transcriptional codes. Nat. Rev. Genet. *1*, 20–29.

Kaiser, T., and Feng, G. (2015). Modeling psychiatric disorders for developing effective treatments. Nat. Med. *21*, 979–988.

Kanton, S., Boyle, M.J., He, Z., Santel, M., Weigert, A., Sanchís-Calleja, F., Guijarro, P., Sidow, L., Fleck, J.S., Han, D., et al. (2019). Organoid single-cell

genomic atlas uncovers human-specific features of brain development. Nature *574*, 418–422.

Kiehn, O. (2006). Locomotor circuits in the mammalian spinal cord. Annu. Rev. Neurosci. *29*, 279–306.

Kiehn, O. (2016). Decoding the organization of spinal circuits that control locomotion. Nat. Rev. Neurosci. *17*, 224–238.

Klapoetke, N.C., Murata, Y., Kim, S.S., Pulver, S.R., Birdsey-Benson, A., Cho, Y.K., Morimoto, T.K., Chuong, A.S., Carpenter, E.J., Tian, Z., et al. (2014). Independent optical excitation of distinct neural populations. Nat. Methods *11*, 338–346.

Koch, S.C., Acton, D., and Goulding, M. (2018). Spinal Circuits for Touch, Pain, and Itch. Annu. Rev. Physiol. *80*, 189–217.

Lai, H.C., Seal, R.P., and Johnson, J.E. (2016). Making sense out of spinal cord somatosensory development. Development *143*, 3434–3448.

Lemon, R.N. (2008). Descending pathways in motor control. Annu. Rev. Neurosci. *31*, 195–218.

Levine, A.J., Lewallen, K.A., and Pfaff, S.L. (2012). Spatial organization of cortical and spinal neurons controlling motor behavior. Curr. Opin. Neurobiol. *22*, 812–821.

Lodato, S., and Arlotta, P. (2015). Generating neuronal diversity in the mammalian cerebral cortex. Annu. Rev. Cell Dev. Biol. *31*, 699–720.

Micali, N., Kim, S.K., Diaz-Bustamante, M., Stein-O'Brien, G., Seo, S., Shin, J.H., Rash, B.G., Ma, S., Wang, Y., Olivares, N.A., et al. (2020). Variation of Human Neural Stem Cells Generating Organizer States In Vitro before Committing to Cortical Excitatory or Inhibitory Neuronal Fates. Cell Rep. *31*, 107599.

Nakano, T., Windrem, M., Zappavigna, V., and Goldman, S.A. (2005). Identification of a conserved 125 base-pair Hb9 enhancer that specifies gene expression to spinal motor neurons. Dev. Biol. *283*, 474–485.

Ogura, T., Sakaguchi, H., Miyamoto, S., and Takahashi, J. (2018). Three-dimensional induction of dorsal, intermediate and ventral spinal cord tissues from human pluripotent stem cells. Development *145*, dev162214.

Pakula, A., Spinazzola, J.M., and Gussoni, E. (2019). Purification of Myogenic Progenitors from Human Muscle Using Fluorescence-Activated Cell Sorting (FACS). Methods Mol. Biol. *1889*, 1–15.

Paşca, S.P. (2018). The rise of three-dimensional human brain cultures. Nature *553*, 437–445.

Paşca, S.P. (2019). Assembling human brain organoids. Science *363*, 126–127.

Paşca, S.P., Portmann, T., Voineagu, I., Yazawa, M., Shcheglovitov, A., Paşca, A.M., Cord, B., Palmer, T.D., Chikahisa, S., Nishino, S., et al. (2011). Using iPSC-derived neurons to uncover cellular phenotypes associated with Timothy syndrome. Nat. Med. *17*, 1657–1662.

Paşca, A.M., Sloan, S.A., Clarke, L.E., Tian, Y., Makinson, C.D., Huber, N., Kim, C.H., Park, J.Y., O'Rourke, N.A., Nguyen, K.D., et al. (2015). Functional cortical neurons and astrocytes from human pluripotent stem cells in 3D culture. Nat. Methods *12*, 671–678.

Philips, T., and Rothstein, J.D. (2015). Rodent Models of Amyotrophic Lateral Sclerosis. Curr. Protoc. Pharmacol. *69*, 5.67.1–5.67.21.

Rosenberg, A.B., Roco, C.M., Muscat, R.A., Kuchina, A., Sample, P., Yao, Z., Graybuck, L.T., Peeler, D.J., Mukherjee, S., Chen, W., et al. (2018). Single-cell profiling of the developing mouse brain and spinal cord with split-pool barcoding. Science *360*, 176–182.

Sala, L., van Meer, B.J., Tertoolen, L.G.J., Bakkers, J., Bellin, M., Davis, R.P., Denning, C., Dieben, M.A.E., Eschenhagen, T., Giacomelli, E., et al. (2018). MUSCLEMOTION: A Versatile Open Software Tool to Quantify Cardiomyocyte and Cardiac Muscle Contraction In Vitro and In Vivo. Circ. Res. *122*, e5–e16.

Sances, S., Bruijn, L.I., Chandran, S., Eggan, K., Ho, R., Klim, J.R., Livesey, M.R., Lowry, E., Macklis, J.D., Rushton, D., et al. (2016). Modeling ALS with motor neurons derived from human induced pluripotent stem cells. Nat. Neurosci. *19*, 542–553.

Sathyamurthy, A., Johnson, K.R., Matson, K.J.E., Dobrott, C.I., Li, L., Ryba, A.R., Bergman, T.B., Kelly, M.C., Kelley, M.W., and Levine, A.J. (2018). Massively Parallel Single Nucleus Transcriptional Profiling Defines Spinal Cord Neurons and Their Activity during Behavior. Cell Rep. *22*, 2216–2225.

Schindelin, J., Arganda-Carreras, I., Frise, E., Kaynig, V., Longair, M., Pietzsch, T., Preibisch, S., Rueden, C., Saalfeld, S., Schmid, B., et al. (2012). Fiji: an open-source platform for biological-image analysis. Nat. Methods *9*, 676–682.

Shi, Y., Lin, S., Staats, K.A., Li, Y., Chang, W.H., Hung, S.T., Hendricks, E., Linares, G.R., Wang, Y., Son, E.Y., et al. (2018). Haploinsufficiency leads to neurodegeneration in C9ORF72 ALS/FTD human induced motor neurons. Nat. Med. *24*, 313–325.

Shim, S., Kwan, K.Y., Li, M., Lefebvre, V., and Sestan, N. (2012). Cis-regulatory control of corticospinal system development and evolution. Nature *486*, 74–79.

Skene, N.G., Bryois, J., Bakken, T.E., Breen, G., Crowley, J.J., Gaspar, H.A., Giusti-Rodriguez, P., Hodge, R.D., Miller, J.A., Muñoz-Manchado, A.B., et al.; Major Depressive Disorder Working Group of the Psychiatric Genomics Consortium (2018). Genetic identification of brain cell types underlying schizophrenia. Nat. Genet. *50*, 825–833.

Sloan, S.A., Darmanis, S., Huber, N., Khan, T.A., Birey, F., Caneda, C., Reimer, R., Quake, S.R., Barres, B.A., and Pasca, S.P. (2017). Human Astrocyte Maturation Captured in 3D Cerebral Cortical Spheroids Derived from Pluripotent Stem Cells. Neuron *95*, 779–790.

Sloan, S.A., Andersen, J., Paşca, A.M., Birey, F., and Paşca, S.P. (2018). Generation and assembly of human brain region-specific three-dimensional cultures. Nat. Protoc. *13*, 2062–2085.

Sousa, A.M.M., Meyer, K.A., Santpere, G., Gulden, F.O., and Sestan, N. (2017). Evolution of the Human Nervous System Function, Structure, and Development. Cell *170*, 226–247.

Steinbeck, J.A., Jaiswal, M.K., Calder, E.L., Kishinevsky, S., Weishaupt, A., Toyka, K.V., Goldstein, P.A., and Studer, L. (2016). Functional Connectivity under Optogenetic Control Allows Modeling of Human Neuromuscular Disease. Cell Stem Cell *18*, 134–143.

Stifani, N. (2014). Motor neurons and the generation of spinal motor neuron diversity. Front. Cell. Neurosci. *8*, 293.

Stuart, T., Butler, A., Hoffman, P., Hafemeister, C., Papalexi, E., Mauck, W.M., 3rd, Hao, Y., Stoeckius, M., Smibert, P., and Satija, R. (2019). Comprehensive Integration of Single-Cell Data. Cell *177*, 1888–1902.

Takuma, H., Sakurai, M., and Kanazawa, I. (2002). In vitro formation of corticospinal synapses in an organotypic slice co-culture. Neuroscience *109*, 359–370.

ten Donkelaar, H.J., Lammens, M., Wesseling, P., Hori, A., Keyser, A., and Rotteveel, J. (2004). Development and malformations of the human pyramidal tract. J. Neurol. *251*, 1429–1442.

Thaler, J., Harrison, K., Sharma, K., Lettieri, K., Kehrl, J., and Pfaff, S.L. (1999). Active suppression of interneuron programs within developing motor neurons revealed by analysis of homeodomain factor HB9. Neuron *23*, 675–687.

Thiry, L., Hamel, R., Pluchino, S., Durcan, T., and Stifani, S. (2020). Characterization of Human iPSC-derived Spinal Motor Neurons by Single-cell RNA Sequencing. Neuroscience, S0306-4522(20)30275-X.

Thomson, S.R., Wishart, T.M., Patani, R., Chandran, S., and Gillingwater, T.H. (2012). Using induced pluripotent stem cells (iPSC) to model human neuromuscular connectivity: promise or reality? J. Anat. *220*, 122–130.

van der Maaten, L., and Hinton, G. (2008). Visualizing Data using t-SNE. J. Mach. Learn. Res. *9*, 2579–2605.

van der Worp, H.B., Howells, D.W., Sena, E.S., Porritt, M.J., Rewell, S., O'Collins, V., and Macleod, M.R. (2010). Can animal models of disease reliably inform human studies? PLoS Med. *7*, e1000245.

Wertz, A., Trenholm, S., Yonehara, K., Hillier, D., Raics, Z., Leinweber, M., Szalay, G., Ghanem, A., Keller, G., Rózsa, B., et al. (2015). PRESYNAPTIC NETWORKS. Single-cell-initiated monosynaptic tracing reveals layer-specific cortical network modules. Science *349*, 70–74.

Wichterle, H., Lieberam, I., Porter, J.A., and Jessell, T.M. (2002). Directed differentiation of embryonic stem cells into motor neurons. Cell *110*, 385–397.

Xiang, Y., Tanaka, Y., Cakir, B., Patterson, B., Kim, K.Y., Sun, P., Kang, Y.J., Zhong, M., Liu, X., Patra, P., et al. (2019). hESC-Derived Thalamic Organoids Form Reciprocal Projections When Fused with Cortical Organoids. Cell Stem Cell *24*, 487–497.

Yoon, S.J., Elahi, L.S., Paşca, A.M., Marton, R.M., Gordon, A., Revah, O., Miura, Y., Walczak, E.M., Holdgate, G.M., Fan, H.C., et al. (2019). Reliability of human cortical organoid generation. Nat. Methods *16*, 75–78.

Zeisel, A., Hochgerner, H., Lonnerberg, P., Johnsson, A., Memic, F., van der Zwan, J., Haring, M., Braun, E., Borm, L.E., La Manno, G., et al. (2018). Molecular Architecture of the Mouse Nervous System. Cell *174*, 999–1014.

Zhou, Q., and Anderson, D.J. (2002). The bHLH transcription factors OLIG2 and OLIG1 couple neuronal and glial subtype specification. Cell *109*, 61–73.